RSC Advances

PAPER

View Article Online
View Journal | View Issue

Cite this: *RSC Adv.*, 2026, **16**, 12037

UPLC-qToF-MS/MS analysis and anti-inflammatory activities of the soft coral *Litophyton savignyi* supported by bioactive molecular networking, network pharmacology, and molecular docking

Shaimaa Fayez,[a] Karim Abed,[a] Mostafa S. Moussa,[a] Lo-Yun Chen,[b] Ting-Wei Liao,[bc] Tsong-Long Hwang,[defg] Po-Jen Chen,[h] Mohamed El-Shazly*[a] and Kuei-Hung Lai *[bcij]

Litophyton savignyi of the Red Sea is one of the underexplored soft corals that is a prolific producer of bioactive metabolites. The anti-inflammatory activity of the hexane fraction of *L. savignyi* was superior to that of the methanol fraction, as revealed by reducing superoxide anion generation (32.05% ± 8.06%) and elastase release in fMLF/CB-induced human neutrophils (96.89% ± 3.69%). The bioactive non-polar fraction was subjected to systematic chemical investigation using UPLC-qToF-MS/MS analysis, and 650 metabolites were found to be exclusively present in the hexane part, of which steroids were the main class representing 26% of all features. Further fractionation of the hexane extract revealed that the polar subfractions ND90-1 and ND90-3 displayed the best inhibition of superoxide generation (96.79% ± 0.16% and 94.27% ± 4.12%, respectively) and elastase release (92.35% ± 2.75% and 91.28% ± 3.41%, respectively). Bioactive molecular networking and multivariate analysis showed that bioactive nodes (r > 0.65 and p < 0.05) and metabolites with top VIP scores (>2) belonged to steroids, sesquiterpenes, fatty amides, and sphingolipids. Network pharmacological studies on these metabolites showed that their hub targets were SRC, PTGS2 (COX-2), HSP90AA1, PPARG, and HIF1A, and they were significantly enriched in inflammatory responses and nuclear receptor–mediated steroid hormone signaling pathways. Molecular docking on COX-2 showed steroids to display scores comparable to those of celecoxib and indomethacin (COX-2 inhibitors as controls), which highlighted the promising anti-inflammatory potential of the hexane extract of *Litophyton savignyi*. Quantitative real-time PCR (qPCR) analysis revealed that the bioactive subfractions reduced the expression of the proinflammatory cytokines IL-6 and IL-1β, hence supporting the involvement of COX-2 mediated anti-inflammatory effect. A detailed analysis on its anti-inflammatory potential requires future *in vivo* investigations.

Received 25th November 2025
Accepted 18th February 2026

DOI: 10.1039/d5ra09089j

rsc.li/rsc-advances

1. Introduction

Inflammation is a highly regulated process that requires proper balance between pro- and anti-inflammatory mediators. While it is an essential response of the immune system to ensure survival during infection and tissue injury, prolonged inflammation could lead to cellular and tissue damages.[1,2] Human leukocyte elastase (HLE) or human neutrophil elastase is a serine protease found in the azurophilic granules of the neutrophils, whose potential substrates are the components of the extracellular matrix and proteins such as clotting factors, complements, immunoglobulins, and cytokines.[3] While suspended in the blood, neutrophils do not cause any damage; however, upon recruitment to the epithelial cells (as in the case of inflammation or infection),[4] they tend to release cytotoxic agents that might be involved in the pathogenesis of inflammatory tissue injury.[3] The release of elastase (actively or

[a]*Department of Pharmacognosy, Faculty of Pharmacy, Ain Shams University, Cairo, Egypt. E-mail: mohamed.elshazly@pharma.asu.edu.eg*
[b]*PhD Program in Clinical Drug Development of Herbal Medicine, College of Pharmacy, Taipei Medical University, Taipei 110301, Taiwan. E-mail: kueihunglai@tmu.edu.tw*
[c]*Graduate Institute of Pharmacognosy, College of Pharmacy, Taipei Medical University, Taipei 110301, Taiwan*
[d]*Center for Drug Research and Development, College of Human Ecology, Chang Gung University of Science and Technology, Taoyuan 333324, Taiwan*
[e]*Graduate Institute of Healthy Industry Technology, College of Human Ecology, Chang Gung University of Science and Technology, Taoyuan 333324, Taiwan*
[f]*Department of Anesthesiology, Chang Gung Memorial Hospital, Taoyuan, 333423, Taiwan*
[g]*Department of Chemical Engineering, Ming Chi University of Technology, New Taipei City, 243303, Taiwan*
[h]*Department of Pharmacology, School of Medicine, College of Medicine, Kaohsiung Medical University, Kaohsiung 80708, Taiwan*
[i]*Traditional Herbal Medicine Research Center, Taipei Medical University Hospital, Taipei 110301, Taiwan*
[j]*National Museum of Marine Biology and Aquarium, Pingtung 944401, Taiwan*

passively) from neutrophils and/or macrophages has been linked to a variety of inflammatory diseases such as rheumatoid arthritis, cystic fibrosis, idiopathic pulmonary fibrosis, chronic obstructive pulmonary disease (COPD), cancer, and adult respiratory distress syndrome.[5–7] Elastases are predictive markers of inflammation; therefore, targeting elastases could potentially reduce inflammation and oxidative stress.[8,9]

Soft corals are essential components of the coral reef ecosystem and are rich sources of bioactive metabolites owing to their sessile nature that warrants defense against other predators.[10] Genus *Litophyton* (genus *Nephthea* was synonymized in 2016 with the genus *Litophyton* due to their identical morphological and genetic features;[11] family: Nephtheidae, order: Alcyonacea, subclass: Octocorallia) is distributed worldwide, especially in the Red Sea, Indo-Pacific region, and Southeast Asia, comprising nearly 100 species.[12–14] They are predominantly rich in sesquiterpenes, cembrane-type diterpenes, nitrogen-containing metabolites, lipids, quinone derivatives, and steroids of the cholestane, ergostane, and pregnane types among others.[12,14] These constituents have been reported to display diverse pharmacological properties including cytotoxic, anti-fouling, antibacterial, antiviral, antifungal, antimalarial, and anti-inflammatory activities.[13,15–18] Steroids are generally the most abundant class of metabolites in *Litophyton* species followed by diterpenes and sesquiterpenes.[10,13] The current advances in untargeted metabolomics have made dereplication of natural extracts more rapid and effective, especially if coupled with bioactivity-guided fractionation. Taxonomically, soft corals encompass three common families in the Red Sea, namely, Alcyoniidae, Nephtheidae, and Xeniidae, of which only Alcyoniidae was well studied.[19,20]

While NSAIDs are one of the oldest and most successful drugs in alleviating pain, fever, and inflammation *via* prostaglandin synthesis inhibition, their detrimental side effects such as gastrointestinal ulcers, serious cardiovascular events, and acute renal failure reduce their patient tolerability and limit their use.[21,22]

As part of our continued search for alternative anti-inflammatory drugs from marine sources, we herein report on the anti-inflammatory activity and the first systematic chemical investigation of the hexane extract of the Red Sea soft coral *Litophyton savignyi* supported by *in silico* tools including bioactive molecular networking, network pharmacology, and molecular docking.

2. Materials and methods

2.1. Collection, authentication, extraction, and fractionation of *Litophyton savignyi*

The soft coral *Litophyton savignyi* was freshly collected off the Red Sea coast 5 km north of Hurghada in October 2023 and it was authenticated by Professor Sayed Abd-ElAziz, a taxonomist at the National Institute of Oceanography and Fisheries (NIOF), Hurghada, Egypt. The fresh sample (1.27 kg, wet weight) was transported in an ice box to the pharmacognosy lab at the faculty of pharmacy, Ain-Shams University, Cairo, Egypt, where it was homogenized, lyophilized and weighted to yield 286.31 g of *L. savignyi* dried weight. The lyophilized sample was ground to a fine brown powder and extracted with 1 : 1 methanol (MeOH) and dichloromethane (DCM) on cold till exhaustion. The coral extract was filtered, concentrated under vacuum to yield a crude total extract of 73.3 g (yield = 25.6%), and finally stored at −20 °C for further analysis. The extract was redissolved in aqueous methanol (9 : 1 MeOH : H_2O) and partitioned with *n*-hexane. The *n*-hexane and aqueous methanol fractions were concentrated to yield 23.0 g and 50.3 g, respectively. The *n*-hexane fraction was subjected to column chromatography on silica gel, using *n*-hexane and DCM (100% hexane, 9 : 1, 8 : 2, 7 : 3, 1 : 1, 6 : 4, 4 : 6, and 2 : 8) and DCM/MeOH mixture (100% DCM, 9 : 1, 8 : 2, 7 : 3, 6 : 4, 4 : 6, and 2 : 8) yielding 42 subfractions that were subjected to thin-layer chromatography and HPLC analysis. Fractions with similar chromatographic patterns were pooled together to yield 9 subfractions, namely, NH-100 (eluted by 100% *n*-hexane), NH-80 (eluted by *n*-hexane : DCM, 8 : 2 v/v), NH-70 (eluted by *n*-hexane : DCM, 7 : 3 v/v), NH-50-1 and NH-50-4 (eluted by *n*-hexane : DCM, 1 : 1 v/v), NH-20 (eluted by *n*-hexane : DCM, 2 : 8 v/v), ND-90-1 and ND-90-3 (both eluted by DCM : MeOH, 9 : 1 v/v), and ND-50 (eluted by DCM : MeOH, 1 : 1 v/v). All subfractions were concentrated and lyophilized for further LC-MS/MS analysis.

2.2. LC-MS/MS data acquisition and processing

All samples for mass spectrometry were prepared at a concentration of 1000 ppm and subsequently filtered through a 0.22 μm PVDF membrane. MS/MS data were collected using a SHIMADZU LCMS-9030 system (SHIMADZU Corporation, Kyoto, Japan) equipped with a Shim-pack GIST C18 column (2 μm, 2.1 mm × 100 mm). The mobile phases consisted of double-distilled water (W, containing 0.1% formic acid) and acetonitrile (A, containing 0.1% formic acid). The gradient elution program is as follows: 0–15 min, 30–100% A; 15–20 min, 100% A. The column temperature was maintained at 40 °C, with a flow rate of 0.4 mL min^{-1}. An injection volume of 5 μL was applied. Mass spectra were acquired in the range of *m*/*z* 100–1800 for non-targeted MS^1 and MS^2 analysis. In MS^2 scans, data-dependent acquisition (DDA) was employed with a collision energy of 35 eV, leading to the fragmentation of the top 5 precursor ions, with a scan time of 0.1 s. Data were collected in the positive ionization mode. The detailed MS parameters were set as follows: interface voltage, 4 kV; nebulizing gas flow, 3.0 L min; heating gas flow, 10 L min; interface temperature, 300 °C; desolvation temperature, 526 °C; drying gas flow, 10 L min; DL temperature, 250 °C; and heat block temperature, 400 °C.

2.3. LC-MS/MS data processing

The raw mass files (.lcd) obtained from the UPLC-qToF-MS/MS were converted to the .mzML format using the MSconvert software. The .mzML files were processed using MZmine 2 for feature finding as follows: mass detection (centroiding, noise level = 1000 for MS^1 and 100 for MS^2); ADAP chromatogram builder (minimum number of scans set to 4, group intensity threshold set to 500, minimum highest intensity set to 20 000,

and m/z tolerance set to 0.005 m/z or 15 ppm); chromatogram deconvolution using local minimum search algorithm (chromatographic threshold was set to 85%, minimum RT range at 0.06, minimum absolute height at 20 000, minimum ratio of peak top to edge at 1.7, and peak duration range at 0.01–2.00 min); isotope removing using isotope grouper algorithm (m/z tolerance was set to 0.005 m/z or 15 ppm, maximum isotope charge at 2, and RT tolerance at 0.04 min); alignment of the detected features across samples using join aligner algorithm (m/z tolerance was set to 0.005 m/z or 15 ppm, weight for m/z at 75%, RT tolerance at 0.25 min, and weight for RT at 25%); and gap filling to add any missed features due to processing (intensity tolerance at 10%, m/z tolerance was set to 0.005 m/z or 15 ppm, and RT tolerance at 0.25 min). Feature filtering was carried out to remove duplicate peaks keeping only the one with the highest intensity across samples (m/z tolerance was set to 0.005 m/z or 15 ppm, and RT tolerance at 0.25 min), and a filter was applied to keep only features present in at least 1 sample. The MS/MS spectra were merged across all samples for aligned features, and the feature list was exported as the feature quantification table (.csv) and MS/MS spectral summary file (.mgf).

2.4. Bioactive molecular networking

A molecular network was created for the nine subfractions using the Feature-Based Molecular Networking (FBMN) workflow on GNPS (https://gnps.ucsd.edu).[23,24] The feature quantification table (.csv) and MS/MS spectral summary file (.mgf) obtained from MZmine 2 along with the metadata file were exported to GNPS for FBMN analysis. The data were filtered by removing all MS/MS fragment ions within ±17 Da of the precursor m/z. MS/MS spectra were window filtered by choosing only the top 6 fragment ions in the ±50 Da window throughout the spectrum. The precursor ion mass tolerance was set to 0.02 Da and the MS/MS fragment ion tolerance to 0.02 Da. A molecular network was created where nodes were only connected by edges when the MS/MS similarity was above a cosine score of 0.7 and more than 6 matched peaks. Edges between two nodes were kept in the network if and only if each of the nodes appeared in each other respective top 10 most similar nodes. The maximum size of a molecular family was set to 0, allowing for maximum clustering without restrictions in cluster size. The spectra in the network were searched against GNPS spectral libraries. The library spectra were filtered in the same manner as the input data. All matches that were kept between the network spectra and the library spectra had a cosine score above 0.6 with at least 6 matched peaks. The DEREPLICATOR was used to annotate the MS/MS spectra. The molecular network was downloaded and visualized on the Cytoscape software v3.10.0. The quantification table file (.csv) obtained from MZmine 2 was edited in Microsoft Excel to contain the bioactivity results of the subfractions (percentage of inhibition of superoxide anion release). The edited quantification table was then uploaded to the "bioactive molecular network" workflow on Jupyter Notebook to calculate the bioactivity score (r values) of every single feature (Pearson's correlation score between bioactivities of mass ions and their relative quantities), along with their significance (P values). The network was allowed to run, and the obtained (.csv) file was downloaded and incorporated into the FBMN in Cytoscape to highlight nodes that might be responsible for the observed bioactivity.

2.5. *In silico* feature annotation

The MS/MS spectral summary file (.mgf) obtained from MZmine 2 was uploaded to SIRIUS (version 5.8) for the analysis of LC-MS/MS data of metabolites. SIRIUS was used to calculate the molecular formula of features based on their MS/MS spectra, and generates fragmentation tree. The CSI:FingerID was used for the *in silico* annotation of features and for providing predicted fingerprint (substructures). The classification of features was achieved using the CANOPUS module and the NPClassifier ontology. The data obtained from the CANOPUS module and NPClassifier were analyzed for understanding the chemodiversity of features that were exclusively detected in the bioactive hexane fraction.

2.6. Multivariate statistical analysis

The feature quantification file (.csv) obtained from MZmine 2 was processed on Microsoft Excel to remove blank features (cutoff = 0.3), and the edited file was uploaded to the MetaboAnalyst 6.0 platform (https://www.metaboanalyst.ca/), where samples were identified as either active or inactive, and scaled using pareto scaling (mean-centered and divided by the range of each variable). Partial least squares-discriminant analysis (PLS-DA) was performed, and the key metabolites discriminating the active and inactive samples were identified based on their variable importance in projection (VIP) scores. The top fifteen metabolites were extracted from MetaboAnalyst and a heatmap was generated using ChiPlot (https://www.chiplot.online/).

2.7. Effects of *Litophyton savignyi* extracts and fractions on superoxide anion generation and elastase release in fMLF/CB-induced human neutrophils

Human neutrophils were collected according to the previously described protocols.[25,26] To assess superoxide anion generation, ferricytochrome c (0.5 mg mL^{-1}) was mixed with a suspension of neutrophils (6×10^5) and preheated at 37 °C for 3 min. To evaluate elastase release, the substrate MeO-Suc-Ala-Ala-Pro-Val-*p*-nitroanilide (0.1 mM) was used under the same conditions. The test sample or 0.1% DMSO (control) was then added and incubated for 5 min, followed by the addition of cytochalasin B (CB) for 3 min. Finally, fMLF (0.1 μM) was added and the reaction was allowed to proceed for 10 min. The absorbance was measured at 550 or 405 nm using a spectrophotometer (Hitachi U-3900, Tokyo, Japan).[27]

2.8. Effects of *Litophyton savignyi* extracts and fractions on ferricytochrome c reduction and elastase substrate cleavage

To evaluate the $O_2^{\bullet-}$-scavenging capacity and the inhibitory ability on elastase activity, experiments were conducted in a cell-free system.[28] The ferric-reducing antioxidant property was evaluated by measuring the reduction of ferric iron (Fe^{3+}) to

ferrous iron (Fe^{2+}).[29] Ferricytochrome *c* (0.6 mg mL^{-1}) or elastase substrate (0.1 mM) was incubated with 0.1% DMSO or the test crude extracts, and changes in absorbance associated with the reduction of ferricytochrome *c* or cleavage of the elastase substrate were continuously monitored at 550 or 405 nm, respectively, in a 4.5 mL cuvette using a spectrophotometer.

2.9. Network pharmacology

2.9.1. Identification of bioactive compounds and target prediction. 3,4-Epoxyguaia-10(12)-3-ene, guaianediol, cyclocolorenone, eudesma-4,7(11)-diene-8-one, confertol, nebrosteroid J, 24-norcholesterol, nephtheasteroid A, and 1-deoxymethylsphinganine were selected for network pharmacological studies based on their high bioactive and VIP scores derived from metabolomic analysis. The Standard InChI (IUPAC International Chemical Identifier) for each compound was retrieved from publicly available chemical databases PubChem (https://pubchem.ncbi.nlm.nih.gov/) and MarinLit (https://marinlit.rsc.org/). The prediction of potential protein targets associated with each bioactive compound was performed using the SwissTargetPrediction tool (https://www.swisstargetprediction.ch/), where targets with probability scores > zero were selected.

2.9.2. Screening of inflammation-related targets. Inflammation-related targets were retrieved using the GeneCards database (https://www.genecards.org/) (accessed on 5th July 2025). The following keywords were used: "inflammation," "oxidative stress," "reactive oxygen species," and "neutrophil activation." The resulting gene lists were merged, and duplicate entries were eliminated. To ensure biological relevance and specificity, only genes with a relevance score of >10 was retained for further analysis. The predicted protein targets of the bioactive compounds were compared with the inflammation-related gene set. The intersection between the two groups was assigned using the Venn diagram tool in SRplot (https://www.bioinformatics.com.cn/srplot).

2.9.3. Analysis of protein–protein interactions (PPIs). To study the interconnectivity of the overlapping inflammation-related targets, a protein–protein interaction (PPI) network was constructed using the STRING database (version 12.0, https://string-db.org/). The intersecting targets were imported into STRING v12.0 with a minimum required interaction score of 0.4 (medium confidence) and "Homo sapiens" as the organism. Disconnected nodes were hidden. The PPI network was exported and visualized in Cytoscape. Centrality parameters (degree, betweenness, and closeness) were calculated using the CytoNCA plugin, and genes scoring above the mean across all metrics were defined as hub genes. Functional modules were identified using the MCODE plugin with default parameters (degree cutoff = 2, node score cutoff = 0.2, *K*-core = 2, max depth = 100).

2.9.4. Functional enrichment analysis. Gene Ontology (GO) and Kyoto Encyclopedia of Genes and Genomes (KEGG) enrichment analyses were conducted using the DAVID 6.8 database (https://davidbioinformatics.nih.gov/). GO analysis was conducted across the three categories, namely biological process (BP), molecular function (MF), and cellular component (CC). For GO and KEGG analyses, a *p*-value threshold of <0.01 was applied to identify statistically significant terms. The top-ranked enriched pathways were integrated and visualized as enrichment bars and bubble plot using SRplot. The network of bioactive compounds–potential targets–signaling pathways was visualized using the Cytoscape v3.10.0 software (Fig. S1).

2.9.5. Hub genes validation. The expressions of hub genes were validated using publicly available microarray datasets from the NCBI Gene Expression Omnibus (GEO, https://www.ncbi.nlm.nih.gov/geo/; accessed on 5th August 2025) database. Inclusion criteria were *Homo sapiens* samples, acute inflammatory conditions, availability of a control group, and expression profiling by array. Differential expression was analyzed using GEO2R, applying the limma package with the Benjamini–Hochberg adjustment for multiple testing. Genes with $|\log_2 FC| > 2$ and an adjusted *P*-value < 0.05 were considered significantly differentially expressed.

2.10. Molecular docking

2.10.1. Ligand preparation. All selected compounds, along with celecoxib and indomethacin as reference inhibitors, were retrieved in 2D format from the PubChem and MarinLit databases. The structures were imported into Avogadro for hydrogenation and energy minimization using the MMFF94 force field. Optimized ligands were saved in .mol2 format and were subsequently processed in AutoDock Tools (ADT) v1.5.7. Gasteiger charges were assigned, polar hydrogens were retained, and the ligands were converted to .pdbqt format for docking.

2.10.2. Protein preparation. The crystal structure of COX-2 (PDB ID: 6COX; 2.80 Å resolution) was retrieved from the RCSB Protein Data Bank (https://www.rcsb.org/). Preprocessing steps involved the removal of water molecules and non-essential chains, with chain A retained for docking. Polar hydrogens were added and Kollman charges were assigned using ADT. The co-crystallized ligand was extracted and redocked into the binding site for the validation of the docking protocol. An RMSD value $\leq$ 2.0 Å was considered acceptable.

2.10.3. Docking process. Docking simulations were performed with AutoDock 4.2 using the Lamarckian genetic algorithm. The grid box was centered on the native ligand binding site with dimensions of 50 × 50 × 50 points and a default spacing of 0.375 Å, covering the active pocket (Table S1). Each ligand was docked in triplicate, with 10 poses generated per run. The lowest-energy conformation from each run was selected, and binding energies were reported as mean ± SD. Protein–ligand interactions were analyzed using Discovery Studio Visualizer v16.1.0.15350.

2.11. Absorption, distribution, metabolism, excretion, and toxicity (ADMET) prediction

Pharmacokinetic characteristics of the selected ligands were evaluated using the pkCSM web server (https://biosig.lab.uq.edu.au/pkcsm/), which applies graph-

based signatures to estimate the ADME parameters. The input structures were provided in the form of SMILES retrieved from the MarinLit and PubChem databases. The platform generated predictions for human intestinal absorption, blood–brain barrier (BBB) permeability, cytochrome P450 enzyme interactions (1A2, 2C19, 2C9, 2D6 and 3A4) and total systemic clearance. Molecular properties and toxicity risks were also examined using the SwissADME prediction tool and the OSIRIS software. Key physicochemical descriptors including partition coefficient (Log *P*), number of hydrogen bond donors and acceptors were computed. These descriptors were used to assess compliance with Lipinski's rule of five, which proposes that orally active compounds typically have ≤5 hydrogen bond donors and ≤10 hydrogen bond acceptors, with a molecular weight of ≤500 Da and log *P* ≤ 5. Moreover, the OSIRIS software was used to predict potential toxicity concerns including mutagenic, tumorigenic, irritant, and reproductive risks based on the structures of the compounds. Additional outputs from OSIRIS include predicting drug-likeness score (based on fragment contributions) and an overall drug score combining pharmacokinetic and toxicity predictions.

2.12. Cell culture, RNA isolation, and quantitative real-time PCR

Human THP-1 cells (BCRC No. 60430) were purchased from the Bioresource Collection and Research Center (BCRC; Hsinchu, Taiwan) and cultured in RPMI 1640 media supplemented with 10% fetal bovine serum, 2 mM L-glutamine, and 1× antibiotic-antimycotic at 37 °C in a humidified incubator with 5% CO_2. THP-1 cells were pretreated with *L. savignyi* methanol and hexane extracts along with the nine hexane subfractions at a final concentration of 10 μg mL^{-1} for 1 h and then activated with or without 200 ng mL^{-1} lipopolysaccharide (LPS; *E. coli* 0111:B4) for another 6 h. Total RNA was extracted using TRIzol reagent (Thermo-Fisher Scientific, Waltham, MA, USA) according to the manufacturer's instructions. cDNA was synthesized from total RNA using the iScript™ cDNA Synthesis Kit (Bio-Rad, Hercules, CA, USA). Quantitative real-time PCR was performed using the Power SYBR™ Green PCR Master Mix on a CFX Connect Real-Time PCR Detection System. Primers for human IL-6 (5′-GGTACATCCTCGACGGCATCT-3′ and 5′-GTGCCTCTTTGCTGCTTTCAC-3′), IL-1β (5′-GCTGAGGAAGATGCTGGTTC-3′ and 5′-AGTTCTGTGGCCGTGTACAA-3′), and GAPDH (5′-GAAGGTGAAGGTCGGAGTC-3′and 5′-GAAGATGGTGATGGGATTTC-3′) were used.

2.13. Statistical analysis

The results are expressed as mean ± S.E.M. Statistical analysis was performed using the GraphPad Prism software (San Diego, USA). A one-way analysis of variance (ANOVA) was conducted, followed by Dunnett's multiple comparison test. A p-value <0.05 was considered statistically significant.

3. Results

3.1. Extraction, fractionation, and bioactive molecular networking

The soft coral sample was extracted with 1 : 1 methanol : DCM (dichloromethane) on cold then subjected to a modified Kupchan partitioning using *n*-hexane and aqueous methanol. The fractions were initially tested for their inhibitory effect on superoxide anion generation and suppression of elastase release in fMLF/CB-induced human neutrophils. As presented in Table 1, the hexane fraction significantly inhibited the generation of superoxide anions and the release of elastase, whereas the methanol fraction was inactive.

Differential LC-MS/MS analysis of the hexane and methanol fractions revealed the presence of nearly 650 chemical components that were exclusively detected in the hexane fraction (Fig. 1A). The chemodiversity and biosynthetic pathways for these 650 metabolites were analyzed using the CANOPUS module in SIRIUS, software for analyzing metabolites from their tandem mass data. The terpenoid pathway was by far the major biosynthetic pathway for the hexane-exclusive secondary metabolites, followed by fatty acids and alkaloids (Fig. 1B). Terpenoids were further analyzed using the NPClassifier of CANOPUS where steroids, diterpenoids, and sesquiterpenoids were the main identified components representing 26%, 22% and 19% of the total identified terpenoids, respectively (Fig. 1C). Fatty acids were similarly analyzed on NPClassifier, where free fatty acids and their conjugates (23%), sphingolipids (18%), glycerolipids (14%), fatty acyls (13%), and fatty amides (13%) represented the major subclasses (Fig. 1D).

In order to identify the components responsible for the bioactivity of the hexane fraction, the latter was further fractionated on a silica gel column to yield 9 subfractions, which were all retested for their superoxide anion and elastase inhibition potential (Table 2). Subfractions ND-90-1 and ND-90-3 displayed the best inhibition for superoxides and elastases, whereas subfractions ND-50, NH-50-1, NH-50-4, and NH-70 displayed moderate inhibitory effects. Subfraction NH-

Table 1 Effects of *Litophyton savignyi* fractions on superoxide anion generation and elastase release in fMLF/CB-induced human neutrophils[a,b]

Sample name	% Inhibition of superoxide anion	% Inhibition of elastase release
Litophyton savignyi methanol extract	−8.75 ± 6.74	−1.12 ± 3.03
Litophyton savignyi hexane extract	32.05 ± 8.06*	96.89 ± 3.69***

[a] Human neutrophils were treated with DMSO (0.1%, as control) or samples for 5 min before adding fMLF/CB for another 10 min. The treating concentration was 10 μg ml^{-1}. [b] Results are presented as mean ± S.E.M. ($n = 3$). *$p < 0.05$, **$p < 0.01$, ***$p < 0.001$ compared with the control.

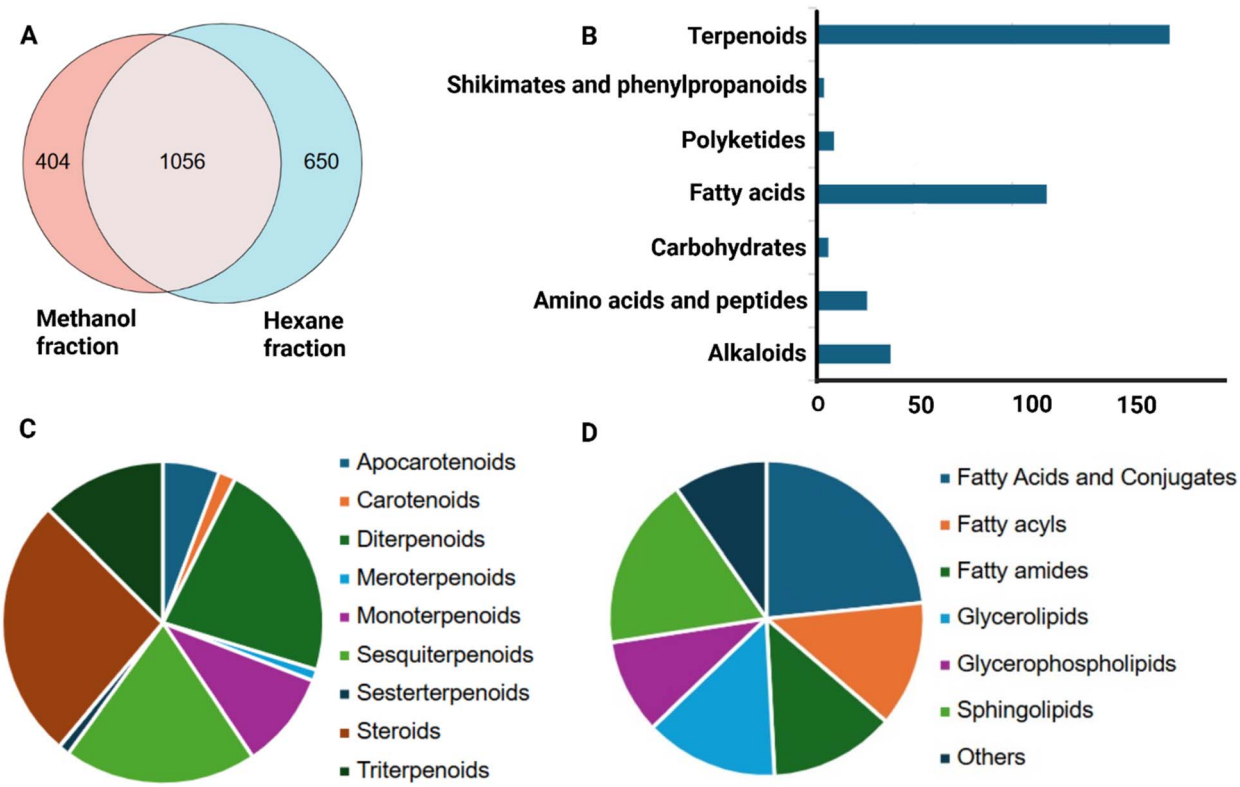

Fig. 1 Chemodiversity of metabolites exclusively detected in the bioactive hexane fraction of *L. savignyi*. (A) Venn diagram illustrating the distribution of metabolites in the hexane and methanol fractions. (B) Biosynthetic pathways of metabolites detected exclusively in the hexane fraction, as analyzed by the CANOPUS module of SIRIUS based on their MS^2 data. (C) Pie chart illustrating the major chemical classes involved in the terpenoids biosynthetic pathway (using the NPClassifier). (D) Pie chart showing the major chemical classes involved in the fatty acids biosynthetic pathway (using the NPClassifier).

80 displayed weak inhibition for superoxide anions yet moderate inhibition for elastases and the *vice versa* was observed for NH-100. Subfraction NH-20 displayed moderate inhibitory effects on superoxide anions yet strong inhibition for elastases. Nevertheless, when evaluated in the cell-free system, none of the subfractions exhibited significant activity.

Table 2 Effects of hexane subfractions on superoxide anion generation and elastase release in fMLF/CB-induced human neutrophils[a,b]

Sample name	% Inhibition of superoxide anion	% Inhibition of elastase release
NH-20	44.89 ± 2.32***	96.82 ± 6.90***
ND-50	31.84 ± 2.87	83.25 ± 13.58
NH-50-1	52.55 ± 2.78***	79.98 ± 4.98***
NH-50-4	66.15 ± 6.75***	81.91 ± 7.40***
NH-70	36.31 ± 6.71**	70.61 ± 4.61***
NH-80	10.63 ± 3.41*	51.62 ± 7.29**
ND-90-1	96.79 ± 0.16***	92.35 ± 2.75***
ND-90-3	94.27 ± 4.12***	91.28 ± 3.41***
NH-100	79.01 ± 4.97***	−6.01 ± 3.85

[a] Human neutrophils were treated with DMSO (0.1%, as control) or samples for 5 min before adding fMLF/CB for another 10 min. The treating concentration was 10 μg ml^{-1}. [b] Results are presented as mean ± S.E.M. ($n = 3$). *$p < 0.05$, **$p < 0.01$, ***$p < 0.001$ compared with the control.

To investigate their chemical profiles, all hexane subfractions were profiled using tandem UPLC-qToF-MS/MS in the positive ion mode. The acquired MS/MS data were preprocessed on MZmine 2 to allow the detection and relative quantification of LC-MS/MS spectral features (ions) across the fractions. The feature-based molecular network (FBMN) was implemented on the GNPS platform for data analysis. The processed data were used to calculate a bioactivity score using Pearson's correlation (r) between the feature intensity (*i.e.*, relative abundance of the molecular ions (peak areas) across the fractions) and the bioactivity (*i.e.*, superoxide anion inhibition) associated with each fraction. The generated bioactive molecular network was imported to Cytoscape for visualization, where nodes with $r > 0.65$ and $p < 0.05$ were considered bioactive metabolites (Fig. 2). Comprehensive dereplication of the MS/MS data of the bioactive hexane subfractions allowed the annotation of 21 metabolites including seven fatty amides (*i.e.*, *N*-acylglycine 14 : 0, palmitamide, *N*-acyl amylamine 12 : 0, *N*-pentadecanoyl-ethanolamine, myristoyl ethanolamide, *N*-acylethanolamine 16 : 3, and palmitoleamide), six sphingolipids (*i.e.*, heptadecasphing-4-enine, 4*E*,8*E*,10*E*-d18 : 3 sphingosine, 15-methylhexadecaphytosphingosine, 9Me,4*E*,8*E*,10*E*-d19 : 3 sphingosine, deoxymethylsphinganine, and galactosylceramide d18 : 2/16 : 1), three sesquiterpenoids (*i.e.*, eudesma-4,7(11)-diene-8-keto or cyclocolorenone, chabrolidione A, and

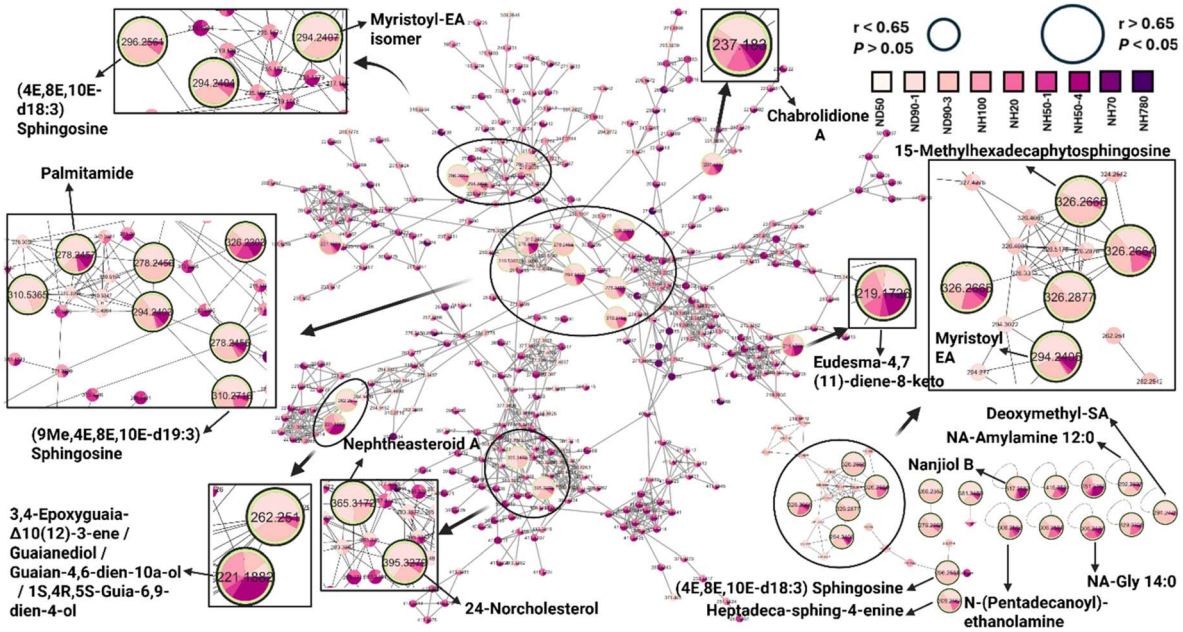

Fig. 2 Bioactive molecular networking of the hexane subfractions of *L. savignyi*, where the node size reflects the bioactivity scores of the mass ions. Node color represents the relative abundance of features across the hexane subfractions. Nodes with bigger size and with black borders are the bioactive nodes ($r > 0.65$ and $p < 0.05$).

guaianediol), and five steroids (*i.e.*, nebrosteroid J, 24-norcholesterol, nephtheasteroid A, nanjiol B, and 24-methylenecholestan-4-ene-3β,6β-diol) (Table 3).

3.2. Identification of compounds in the bioactive hexane subfractions using UPLC-qToF-MS/MS

3.2.1. Steroids. Steroids are the major chemical constituents present in soft corals especially in the Nephtheidae family. Their wide distribution in corals is attributed to the symbiotic relationship with intracellular algae named zooxanthellae,[14] besides the complex food web. In our study, six steroids were identified (peaks 17–23 at t_R 9–14 min) (Table 3), as highlighted by the bioactive molecular network (Fig. 2). The identification of compounds was based on the molecular formula and databases like Marinlit as well as the interpretation of their MS/MS data, which showed characteristic fragments corresponding to dehydration (−18 Da), loss of the alkyl side chain attached to C-17, the cleavage of pentyl ring D, and the subsequent loss of C_2H_2 moieties (−26 Da). All identified steroids belonged to the cholestane series except for a single C-26 norcholestane steroid (peak 18) at *m*/*z* 395.3279 (t_R = 11.90 min), which was identified as 24-norcholesterol with a molecular formula of $C_{26}H_{44}O$ [M + Na]$^+$, whose MS/MS spectra showed a fragment at *m*/*z* 297 corresponding to the loss of a C_7H_{14} moiety of the alkyl side chain attached to C-17 of the pentyl ring (−98 Da) followed by subsequent dehydration (−18 Da) to give a fragment at *m*/*z* 279. The fragmentation of the pentyl ring along C13–C17 and C14–C15 was presented with the fragment at *m*/*z* 237 through the loss of C_3H_6 (−42 Da) followed by the sequential loss of C_2H_2 (−26 Da), which is characteristic for the steroidal nucleus.[30,31] To further confirm the annotation of the compound, the CSI:FingerID generated in SIRIUS (which represents binary vectors of fixed length where each bit describes the presence or absence of a specific substructure) was used. Analysis of the predicted fingerprint revealed the presence of an 18-carbon ring system of the 3-hydroxy steroid, which correlates with the structure of 24-norcholesterol. Neptheasteroid A (peak 19, t_R = 11.93 min) (Table 3), an oxygenated cholestane steroid previously isolated from *Nephthea erecta* off the coast of south Taiwan,[32] showed a molecular formula of $C_{27}H_{42}O$. Its MS/MS spectra displayed the same pattern of fragmentation as that of 24-norcholesterol with the initial loss of an C_9H_{16} alkyl side chain (−124 Da) at *m*/*z* 241, followed by the fragmentation of the pentyl ring at *m*/*z* 199 through the loss of a C_3H_6 moiety (−42 Da), and the sequential loss of C_2H_2 (−26 Da). The CSI:FingerID showed the same characteristic 18-carbon ring system fingerprint of steroids. Peak 21 was identified as 24-methylenecholestan-4-ene-3β,6β-diol, a cholestane steroid that has previously been isolated from *Nephthea* sp. collected from the Xisha Islands of the South China Sea.[33] It was identified as a 3,6-dihydroxy steroid, which correlates with the proposed structure. The observed MS/MS spectra matched with that reported in the literature,[33] showing the initial loss of two water molecules (−18 Da) at *m*/*z* 379 followed by the loss of a $C_{11}H_{22}$ moiety (−154 Da) at *m*/*z* 243. Peak 22 (t_R = 13.65 min) at *m*/*z* 451.3161 was tentatively identified as nebrosteroid J corresponding to the molecular formula $C_{28}H_{44}O_3$ [M + Na]$^+$ with MS/MS fragmentation at *m*/*z* 203 attributed to the neutral loss of a $C_{15}H_{20}O_3$ moiety (−248 Da), which subsequently lost C_3H_{10} (−46 Da) to yield a fragment at *m*/*z* 157. Analysis of the predicted fingerprint from CSI:Finger ID revealed the presence of a methoxycarbonyl moiety, which was consistent with the structure of nebrosteroid J. A previous study has reported on a promising wound healing

Table 3 Annotation of key bioactive metabolites in the hexane subfractions of *L. savignyi*[a]

Peak no.	t_R (min)	Annotation	Experimental *m*/*z*	Δ(ppm)	Molecular formula	Nominal mass	SIRIUS score	CANOPUS ID	MS/MS
1	0.54	NA-Gly 14 : 0	308.2196 $[M + Na]^+$	0.14	$C_{16}H_{31}NO_3$	285	100%	Fatty amides	308, 290, 231
2	0.56	Palmitamide	278.2455 $[M + Na]^+$	0.25	$C_{16}H_{33}NO$	255	100%		278, 260, 159, 133, 105
3	0.57	Heptadecasphing-4-enine (sphingosine d17 : 1)	308.2560 $[M + Na]^+$	0.01	$C_{17}H_{35}NO_2$	285	100%	Sphingolipids	308, 290, 245
4	1.14	(4*E*,8*E*,10*E*-d18 : 3) sphingosine	296.2561 $[M + H]^+$	−7.75	$C_{18}H_{33}NO_2$	295	100%		381, 325, 279, 269, 251, 213, 181, 173, 155, 128, 115
5	1.60	*N*-acyl amylamine 12 : 0	292.2607 $[M + Na]^+$	−1.19	$C_{17}H_{35}NO$	269	100%	Fatty amides	292, 204, 159, 145, 133, 117, 105
6	1.64	15-Methylhexadeca phytosphingosine	326.2665 $[M + Na]^+$	−1.84	$C_{17}H_{37}NO_3$	303	90%	Sphingolipids	326, 294, 203, 163, 145, 133, 119, 105
7	1.99	*N*-(Pentadecanoyl)-ethanolamine	308.2562 $[M + Na]^+$	0.53	$C_{17}H_{35}NO_2$	285	100%	Fatty amides	308, 263, 245
8	2.18	Myristoyl-ethanolamine	294.2405 $[M + Na]^+$	0.53	$C_{16}H_{33}NO_2$	271	100%		294, 249, 231
9	3.01	*N*-Acylethanolamine 16 : 3	294.2430 $[M + H]^+$	0.85	$C_{18}H_{31}NO_2$	293	100%		294, 276, 215, 175, 147, 131, 105
10	3.53	Eudesma-4,7(11)-diene-8-keto/(+)-cyclocolorenone	219.1726 $[M + H]^+$	−10.6	$C_{15}H_{22}O$	218	95%	Sesquiterpenoids	219, 201, 175, 161, 159, 145, 131, 119, 105
11	3.53	Chabrolidione A/confertol	237.183 $[M + H]^+$	−10.2	$C_{15}H_{24}O_2$	236	99%		237, 219, 201, 177, 161, 147, 133, 119, 107
12	3.8	(9Me,4*E*,8*E*,10*E*-d19 : 3) sphingosine	310.2713 $[M + H]^+$	−8.7	$C_{19}H_{35}NO_2$	309	99%	Sphingolipids	310, 217, 161, 147, 133, 119, 105
13	3.95	Deoxymethyl-SA	294.2775 $[M + Na]^+$	−0.68	$C_{17}H_{37}NO$	271	85%		294, 161, 135, 119, 103
14	5.37	Unidentified	260.2352 $[M + Na]^+$	−0.84	$C_{16}H_{31}N$	237	100%	Sesquiterpenoids	260, 215, 173, 159, 143, 131, 116
15	5.63	Palmitoleamide	276.2303 $[M + Na]^+$	1.88	$C_{16}H_{31}NO$	253	100%	Fatty amides	235, 215, 173, 157, 145, 131, 117
16	6.98	3,4-Epoxyguaia-Δ10(12)-3-ene/ Guaianediol/Guaian-4,6-dien-10a-ol/1S,4R,5S-Guia-6,9-dien-4-ol	221.1882 $[M + H]^+$	−10.5	$C_{15}H_{24}O$	220	97%	Sesquiterpenoids	221, 203, 161, 135, 119, 105
17	9.61	Nebrosteroid J	429.3328 $[M + H]^+$	−9.40	$C_{28}H_{44}O_3$	428	100%	Steroids	429, 393, 353, 241
18	11.90	24-Norcholesterol	395.3279 $[M + Na]^+$	−1.34	$C_{26}H_{44}O$	372	100%		395, 297, 279, 237, 211, 185, 159, 133
19	11.93	Nephtheasteroid A	365.3172 $[M - H_2O + H]^+$	−9.58	$C_{27}H_{42}O$	382	100%		365, 241, 199, 173, 147, 121
20	12.57	Nanjiol B	517.3582 $[M + H]^+$	10.20	$C_{31}H_{48}O_6$	516	45%		—
21	13.48	24-Methylenecholestan-4-ene-3β,6β-diol	415.3530 $[M + H]^+$	−11.15	$C_{28}H_{46}O_2$	414	100%		415, 379, 253, 213, 199
22	13.64	Nebrosteroid J	451.3161 $[M + Na]^+$	−6.02	$C_{28}H_{44}O_3$	428	100%		451, 203, 157
23	14.35	Unidentified	381.3483 $[M + Na]^+$	−3.72	$C_{26}H_{46}$	358	51%		299, 189, 161, 145, 135, 119, 105
24	16.72	GalCer (d18 : 2/16 : 1)	696.5341 $[M + H]^+$	−9.76	$C_{40}H_{74}N_1O_8$	695	—	Sphingolipids	GNPS match library spectrum

[a] All annotations were made by integrating multiple databases including MarinLit and metabolomics workbench with untargeted metabolomics tools such as SIRIUS, NPClassifier, and GNPS.

activity of Red Sea-collected *Nephthea* sample owing to its richness in steroids, which regulated the proinflammatory cytokines NF-κB, TNF-α, IL-6, and IL-1β in the *in vivo* model.[34] Another *Nephthea* steroid has shown gastroprotective effects in rat models with gastric ulcer *via* controlling the PI3K signaling pathway.[35] Our results were also in agreement with previously published data on the anti-inflammatory properties of the 4-methylated steroids, nebrosteroids A–H, isolated from the acetone fraction of the Formosan soft coral *Nephthea chabroli*.[36] The ethyl acetate extract of *Nephthea* species collected from Saponda Island exhibited anti-inflammatory and immunomodulatory activities *in vivo* owing to its steroidal content.[37]

3.2.2. Sesquiterpenoids. Sesquiterpenoids were likewise identified in the hexane extract of *L. savignyi*. A common fragmentation pattern was observed across all identified sesquiterpenes, including the loss of a water molecule (−18 Da), followed by the loss of either C_3H_6 (−42 Da) or C_3H_6O (−58 Da) moieties, and a C_2 hydrocarbon fragment corresponding to the neutral loss of acetylene (−26 Da), ethylene (−28 Da), or ethane (−30 Da). Peak 11 displayed an *m*/*z* at 237.1830 (t_R = 3.53 min) corresponding to the molecular formula $C_{15}H_{24}O_2$ $[M + H]^+$ and it was annotated as chabrolidione A, a compound previously isolated from the Formosan soft coral *N. chabroli*[38], or as confertol, a humulane-sesquiterpenoid previously isolated form *N. albida* (*Litophyton savignyi*). Its MS/MS spectra showed loss of a water molecule at *m*/*z* 219, followed by the fragmentation of the butanoyl side chain at *m*/*z* 161, and the loss of an ethylene group at *m*/*z* 133. Peak 10 is highlighted by the bioactive network with *m*/*z* at 219.1726 (t_R = 3.53 min) corresponding to the molecular formula $C_{15}H_{22}O$ $[M + H]^+$, and it was similarly classified as a sesquiterpene. Its elemental composition corresponded to either the guaiane-type compound cyclocolorenone, which has previously been isolated from *Nephthea* sp. in the Indian ocean,[39] or to the eudesmane-type terpene eudesma-4,7(11)-diene-8-one.[40] Both isomers are ketones and exhibit nearly identical fragmentation patterns, making it difficult to differentiate between them solely on MS/MS. The MS^2 spectrum of peak 10 followed the same pattern described previously, therefore supporting a common skeleton and functional groups. Peak 16 showed an *m*/*z* value at 221.1880 (t_R = 5.59 min) corresponding to the molecular formula $C_{15}H_{24}O$ $[M + H]^+$. It displayed the highest bioactivity score (0.714) among the identified sesquiterpenes, making it a high-priority target for further investigation. There are six known sesquiterpenoids, having this same molecular formula, which have previously been isolated from *Nephthea* sp.[41,42] Among them, two sesquiterpenoids, namely, eudesma-4,7(11)-diene-8β-ol and 8β-hydroxyprespatane, were excluded since their MS/MS fragments were inconsistent with those reported in the literature.[42] The four remaining ones were the guaiane-type sesquiterpenes guaianediol, 3,4-epoxyguaia-Δ10(12)-3-ene, guaian-4,6-dien-10a-ol, and 1S,4R,5S-guia-6,9-dien-4-ol, whose fragmentation aligned with the those observed for sesquiterpenoids. Our results were in agreement with those reported on other *Nephthea* species from the Red Sea, yet collected from Sharm El-Sheikh, showing terpenoids, especially for sesquiterpenes, as COX-2 inhibitors with potential anti-inflammatory properties.[43] The bioactive terpenoids were concentrated in the petroleum ether and acetone fractions, which displayed the highest activity. Cembrane diterpenes from the cultured soft coral *Nephthea columnaris* were likewise reported to display anti-inflammatory properties through the inhibition of the accumulation of the pro-inflammatory iNOS and COX-2 protein in lipopolysaccharide (LPS)-stimulated RAW264.7 macrophages.[44]

3.2.3. Fatty amides. Soft corals are rich in lipids like fatty amides, which are considered as "signatures" of coral bleaching since they are downregulated during thermal stress.[45] Seven fatty amides were identified including palmitamide (peak 2, t_R = 0.56 min) and its unsaturated analogue palmitoleamide (peak 15, t_R = 5.63 min) with *m*/*z* values at 278.2455 and *m*/*z* 276.2303, respectively. Palmitamide, which has been reported to possess anti-inflammatory activity,[46] showed MS^2 fragments at *m*/*z* 260 (due to an initial dehydration step), at *m*/*z* 159 (arising from the loss of a $C_6H_{15}N$ moiety (−101 Da) through carbon–carbon cleavage), and at *m*/*z* 133 and *m*/*z* 105 due to the loss of smaller hydrocarbon moieties. Peak 1 had an $[M + Na]^+$ adduct ion at *m*/*z* 308.2196 (t_R = 0.54 min), and was identified as *N*-myristoyl glycine corresponding to the molecular formula $C_{16}H_{31}NO_3$. Its MS/MS spectra showed the loss of water at *m*/*z* 290 followed by the loss of C_2H_5NO (−59 Da) at *m*/*z* 231 consistent with the loss of a deoxygenated glycine moiety. Three acylethanolamines (peaks 7–9) were putatively identified at t_R ranging from 1.9 to 3.0 min, namely *N*-(pentadecanoyl)-ethanolamine at *m*/*z* 308.2562, myristoylethanolamine at *m*/*z* 294.2405, and *N*-acylethanolamine 16 : 3 at *m*/*z* 294.2430. Their MS/MS spectra showed the characteristic loss of either a C_2H_7NO ethanolamine moiety (−61 Da) or the loss of a C_2H_7N moiety (−45 Da) followed by dehydration (−18 Da).

3.2.4. Sphingolipids. Sphingolipids are structural components that play an essential role in membrane formation, cellular interactions and signal transduction. A glycosphingolipid (peak 24, t_R = 16.72 min) was tentatively identified by GNPS as galactosylceramide d18 : 2/16 : 1. The annotation was of high confidence (cosine score = 0.87) with 8 matched peaks between the experimental data and the library data. The MS/MS spectra showed a fragment at *m*/*z* 516 attributed to the loss of galactose (−180 Da). Furthermore, five sphingoid bases were identified in the current study, among them was peak 3 (*m*/*z* 308.2560, t_R = 0.57 min) that was identified as sphingosine d17 : 1 ($C_{17}H_{35}NO_2$ $[M + Na]^+$) with MS^2 fragments at *m*/*z* 290 and 245 attributed to the loss of water (−18 Da) and C_2H_7N molecules (−45 Da), respectively.

3.3. Multivariate data analysis of the active *vs.* inactive subfractions

To further verify the results obtained from the bioactive molecular network and to prioritize the identified metabolites for further testing, we performed partial least squares-discriminant analysis (PLS-DA) (R^2 = 0.82 and Q^2 = 0.69), a supervised multivariate method for classification and dimensionality reduction, hence reducing the complexity of data by reducing noise. The score plot demonstrated clear separation between the active (*i.e.*, NH100, NH50-4, ND90-1 and

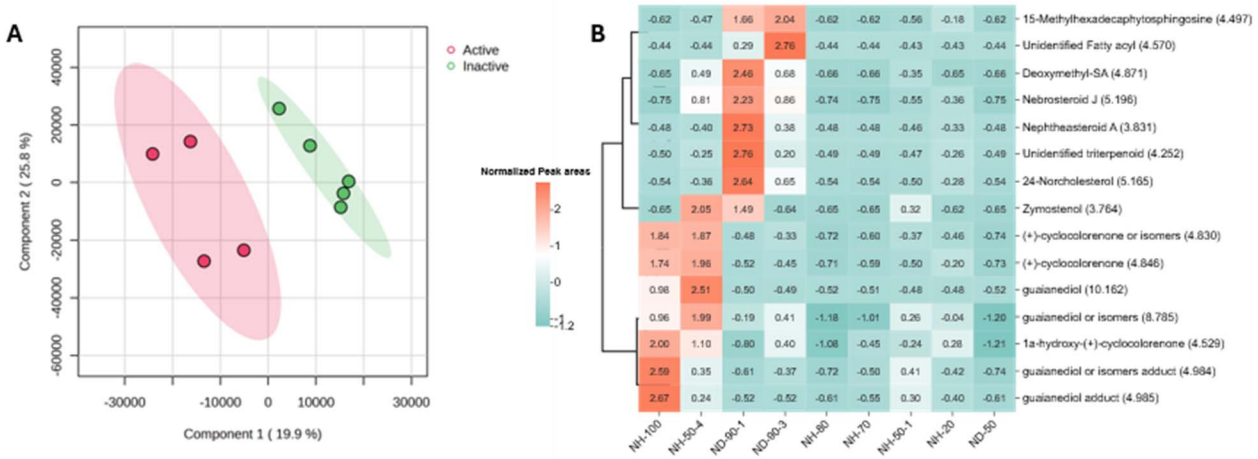

Fig. 3 Multivariate statistical analysis of the hexane subfractions of *L. savignyi*. (A) PLS-DA score plot of the active *vs.* inactive hexane subfractions. The active subfractions are NH100, NH50-4, ND90-1 and ND90-3, while the remaining subfractions are classified as inactive. (B) Heatmap of the top 15 VIP metabolites showing their relative abundance and their VIP scores across the hexane subfractions (extracted using MetaboAnalyst).

ND90-3) and inactive hexane subfractions (Fig. 3) along the first principal component, indicating different chemical profiles between the two groups reflecting their different bioactivities.

Since the two groups were well-separated, we examined the variable importance in projection (VIP) score along the first principal component to identify the discriminating metabolites between the two groups responsible for the observed bioactivity. The top 15 metabolites (VIP > 2), of which 12 were annotated as terpenes (primarily sesquiterpenes), were highly abundant in the active hexane subfractions (Fig. 3B). Steroids and fatty acyls showed higher relative abundance (normalized peak areas) in the active ND90-1 and ND90-3 subfractions, while sesquiterpenoids showed higher abundance in the active NH100 and NH50-4 subfractions. Compounds detected by bioactive molecular networking that have high VIP scores are presented in Fig. 4, and they were subjected to network pharmacological studies to understand their possible targets and the biological pathways they probably affect during oxidative stress and inflammation.

3.4. Network pharmacology

3.4.1. Identification of bioactive compounds and target prediction. The number of predicted targets for each compound is as follows: 3,4-epoxyguaia-10(12)-3-ene (1 target), guaianediol (34), cyclocolorenone (29), eudesma-4,7(11)-diene-8-one (41), confertol (2), nebrosteroid J (78), 24-norcholesterol (46), nephtheasteroid A (26), and 1-deoxymethylsphinganine (17). After merging the individual target lists and removing duplicate

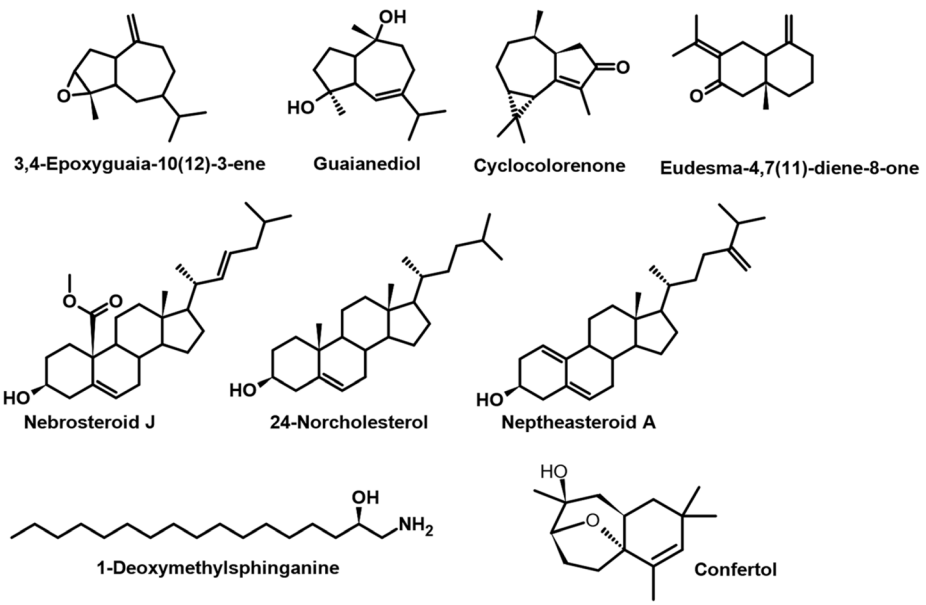

Fig. 4 Compounds with high bioactivity score ($r > 0.65$ and $p < 0.05$) and high VIP scores (>2) identified in the active hexane subfractions against superoxide anions.

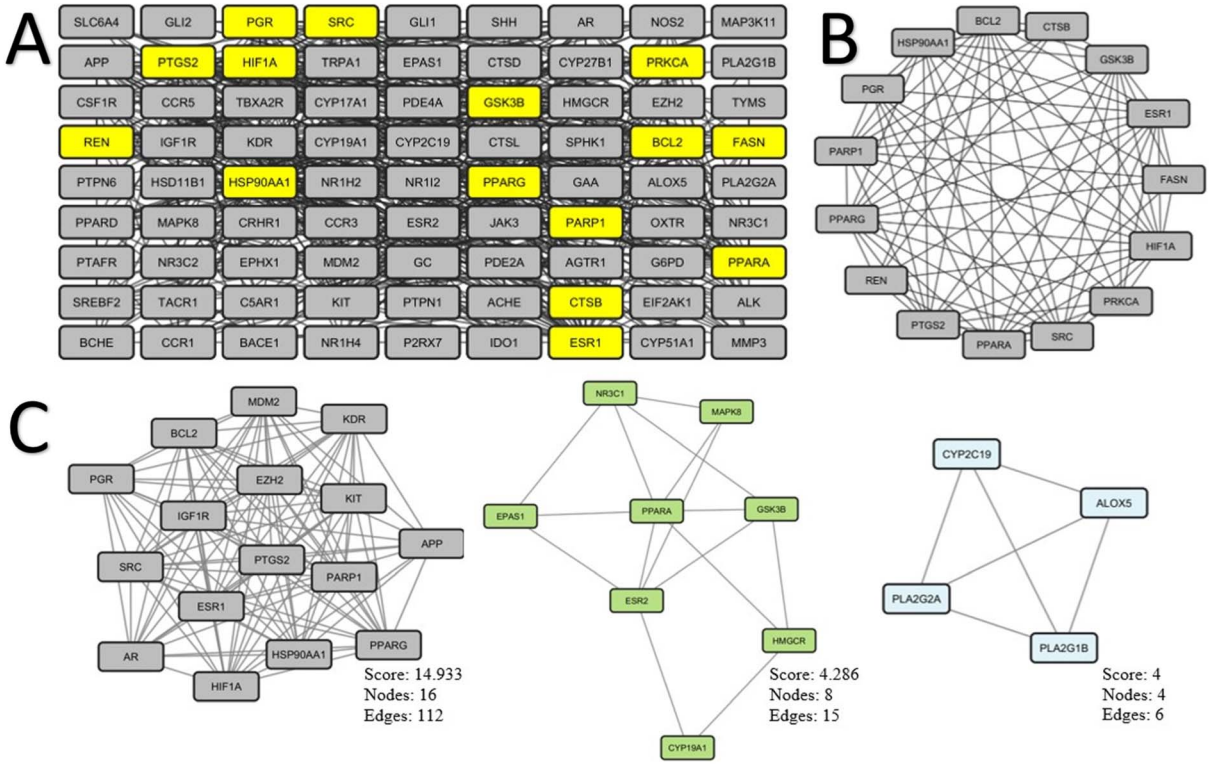

Fig. 5 (A) PPI network highlighting the core hub genes potentially involved in modulating the anti-inflammatory mechanisms of selected bioactive compounds in the hexane fraction of *L. savignyi*. (B) Subnetwork showing hub gene interconnectivity. (C) Top three MCODE clusters with cluster 1 being the most densely connected with the highest biological significance in modulating inflammation.

entries, a total of 165 compound-associated targets were obtained.

3.4.2. Screening of inflammation-related targets. A total of 2072 inflammation-related genes were obtained, of which 82 were common with those of the bioactive compounds, therefore they might play a key role in mediating the anti-inflammatory effects of these compounds. Notably, no overlapping targets were identified for 3,4-epoxyguaia-10(12)-3-ene, whereas the remaining compounds shared main common targets with enzymes, receptors, and kinases (Fig. S2).

3.4.3. Protein–protein interaction (PPI) network. The constructed PPI network (Fig. 5A) had 81 nodes (after excluding one node that was not connected), 588 edges, an average node degree of 14.3, an average local clustering coefficient of 0.56, and a significant PPI enrichment (p-value $< 1.0 \times 10^{-16}$), indicating that the identified targets were functionally connected. A total of 15 hub genes were identified based on topological scoring (DC, BC, and CC), and a subnetwork highlighting their interactions was constructed (Fig. 5B and Table 4). This core subnetwork consisted of 15 nodes and 88 edges, reflecting a tightly connected cluster of proteins that may serve as key regulators in the anti-inflammatory mechanisms of these bioactive compounds. The MCODE analysis identified six functional clusters within the PPI network. The top three were selected (Fig. 5C) where clusters 1, 2, and 3 showed MCODE scores of 14.933, 4.286, and 4, respectively. Cluster 1 was the most densely connected and biologically significant, where nine of its nodes overlapped with the hub genes (including the five highest-ranked hubs: SRC, PTGS2, HSP90AA1, PPARG, and HIF1A). Therefore, this cluster likely represents a core regulatory module mediating the anti-inflammatory effects of the selected bioactive compounds and was prioritized for molecular docking analysis.

Table 4 Topological analysis of hub genes in the constructed PPI network. Degree centrality (DC), betweenness centrality (BC), and closeness centrality (CC) values were calculated to identify key regulators of inflammation

Hub gene	BC	CC	DC	Category
SRC	1141	0.24 767 068	29.502	Kinase
PTGS2	833	0.23551	25.765	Oxidoreductase
HSP90AA1	419	0.24 146 667	27.24	Cytosolic protein
PPARG	359	0.2 361 415	26.019	Nuclear receptor
HIF1A	322	0.23 977 117	25.899	Transcription factor
PPARA	266	0.21 93205	14.967	Nuclear receptor
ESR1	238	0.24 141 839	27.397	Nuclear receptor
GSK3B	203	0.22 820 592	18.31	Kinase
BCL2	170	0.24 137 156	26.991	Ion channel
REN	168	0.20 510 371	10.427	Protease
CTSB	140	0.20 599 568	10.926	Protease
PRKCA	134	0.21 617 016	9.891	Kinase
PARP1	132	0.21 336 937	13.744	Enzyme
FASN	94	0.20 831 807	11.944	Transferase
PGR	89	0.22 568 119	16.451	Nuclear receptor

Src, a non-receptor tyrosine kinase, plays a pivotal role in inflammation by regulating immune cell function and vascular dynamics.[47] It is involved in the recruitment and activation of monocytes, macrophages, neutrophils, and other innate immune cells. Besides its role in promoting vascular permeability during inflammatory responses, Src contributes to key immunological processes such as immune cell differentiation, proliferation, adhesion, migration, chemotaxis, phagocytosis, and survival.[47,48] It also serves as a central modulator of reactive oxygen species (ROS) production and overall cellular homeostasis.

Prostaglandin-endoperoxide synthase 2 (PTGS2), also known as cyclooxygenase-2 (COX-2), is a key rate-limiting enzyme involved in the conversion of arachidonic acid into prostaglandins following cellular injury.[49] During inflammation, COX-2 is typically upregulated, leading to increased prostaglandin production, which modulate vascular tone, platelet aggregation, pain perception, and the overall inflammatory response.[50]

Heat shock protein 90 alpha family class A member 1 (HSP90AA1) functions as a stress-responsive chaperone that contributes to inflammation and oxidative stress regulation by stabilizing signaling proteins.[51] It plays a critical role in regulating autophagy, which is a cellular degradation process that influences oxidative stress, inflammation, and programmed cell death. Prolonged exposure to reactive oxygen species (ROS) has been shown to enhance HSP90 secretion from endothelial cells as it acts as a chemotactic factor by promoting the migration of monocytes during oxidative and inflammatory stress.[52]

PPAR-γ activation promotes cellular differentiation, induces apoptosis, and halts cell cycle progression. It plays a key role in suppressing inflammation, oxidative stress, angiogenesis, and abnormal cell proliferation, invasion, and migration.[53] The upregulation of PPAR-γ exerts anti-inflammatory effects largely through downregulation of pro-inflammatory mediators such as TNF-α and NF-κB, while also mitigating oxidative stress responses.[53]

Hypoxia promotes ROS accumulation, thereby exacerbating oxidative stress. ROS facilitates the stabilization of HIF1A by inhibiting prolyl hydroxylases (PHDs), allowing HIF1A to accumulate in the nucleus, where it binds to hypoxia response elements (HREs) and modulates the transcription of genes involved in erythropoiesis, angiogenesis, metabolic reprogramming, cell proliferation, apoptosis, and survival under low-oxygen conditions.[54]

3.4.4. Functional enrichment analysis. To elucidate the functional roles of the 82 intersecting target genes, GO and KEGG enrichment analyses were performed. A total of 136 GO terms with a p-value < 0.01 were identified, including 51 biological process (BP) terms, 27 cellular component (CC) terms, and 58 molecular function (MF) terms. The top five GO terms from each category were visualized in Fig. 6A.

The most significantly enriched biological processes were inflammatory response, nuclear receptor–mediated steroid hormone signaling pathway, and intracellular receptor signaling pathway. In the CC category, notable terms included the plasma membrane, receptor complex, and chromatin, whereas for the MF, the most enriched terms were nuclear receptor activity, sequence-specific DNA binding, and enzyme binding.

KEGG pathway analysis was conducted (Fig. 6B), where all pathways with p-values < 0.01 were ranked based on their significance. The top five pathways were prolactin signaling, efferocytosis, EGFR tyrosine kinase inhibitor resistance, VEGF signaling, and arachidonic acid metabolism, which were shown to be potentially involved in mediating the anti-inflammatory effects of the selected compounds.

The prolactin signaling pathway plays a multifaceted role in modulating immune responses and has been implicated in the pathogenesis of various inflammatory diseases.[55] Further inspection of its components reveals coordinated regulation of several genes such as SRC, MAPK8, JNK, and GSK3B that intersect with key inflammatory signaling cascades such as the

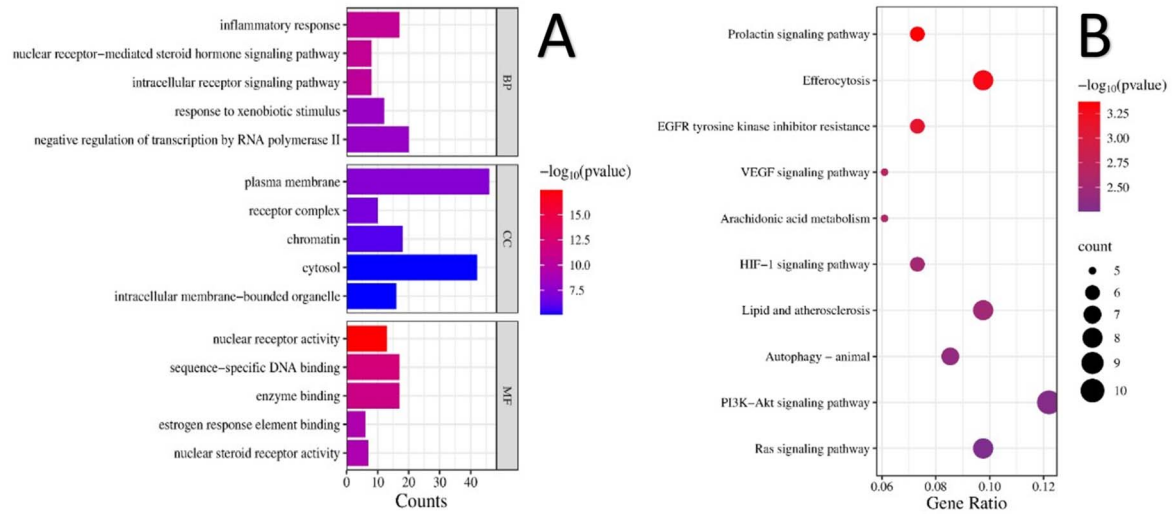

Fig. 6 Enrichment analysis of (A) GO terms like BP, CC, and MF (top 5 ranked in each category based on their significance) and (B) KEGG pathways showing the top enriched signaling (p < 0.01).

PI3K/Akt and MAPK pathways, which contribute significantly to LPS-induced inflammatory responses in macrophages by regulating key inflammatory processes and mediators such as NF-kB, AP-1 and iNOS.[56]

Efferocytosis, a process by which macrophages clear apoptotic cells, plays a critical role in the resolution of inflammation by promoting the secretion of anti-inflammatory cytokines, such as TGF-β and IL-10, which suppress the production of pro-inflammatory mediators.[57] By physically sequestering dying cells, efferocytosis also limits the release of intracellular damage-associated molecular patterns (DAMPs) that can amplify inflammation.[58] Therefore, efferocytosis is essential for preventing excessive inflammatory responses and facilitating tissue repair, hence protecting against inflammatory conditions.[59]

The EGFR tyrosine kinase inhibitor resistance pathway intersects with the PI3K-Akt and JAK-STAT pathways.[60] The activation of SRC and JAK stimulates both pathways primarily through the phosphorylation and activation of STAT3, which drives the transcription of inflammation-related genes.[61] Almost all cytokines activate the JAK-STAT pathway, which plays an important role in inflammatory processes.[62]

Additional relevant pathways include VEGF signaling, arachidonic acid metabolism, and HIF-1 signaling pathways, all of which are directly implicated in inflammatory processes. KEGG pathway analysis highlights that in VEGF signaling, VEGFR regulates both SRC and COX-2, ultimately promoting prostaglandin production. It also intersects with arachidonic acid metabolism through the regulation of COX-2, 5-lipoxygenase, and phospholipase A2, which are key enzymes in the biosynthesis of inflammatory mediators. Hypoxic conditions induce SRC-dependent signaling cascades and expression of HIF-1A, which are both closely associated with angiogenesis by upregulating VEGF expression.[63]

3.5. Hub genes validation

Three GEO datasets met the inclusion criteria (described in methodology section 2.9.5.) including GSE2322, GSE198326 and GSE40885 (Table S2). Each contained both untreated control and lipopolysaccharide (LPS)-induced inflammatory samples. The numbers of differentially expressed genes (DEGs) identified were 45, 489, and 151 for GSE2322, GSE198326, and GSE40885, respectively (Fig. S3). Three GEO datasets met the inclusion criteria (described in section 2.9.5.) including GSE2322, GSE198326 and GSE40885 (Table S2). Each contained both untreated control and lipopolysaccharide (LPS)-induced inflammatory samples. The numbers of differentially expressed genes (DEGs) identified were 45, 489, and 151 for GSE2322, GSE198326, and GSE40885, respectively (Fig. S3). A Venn diagram was constructed between the three datasets (Fig. S3), which revealed 10 common DEGs (Table 5), of which PTGS2 (COX-2) was consistently and significantly upregulated; however, other hub genes did not meet the statistical cutoffs in any of the datasets. Given the convergence between transcriptomic data and literature evidence, PTGS2 was prioritized for downstream molecular docking.

3.6. Molecular docking

The validation of the docking protocol was confirmed with redocking of the native ligand, yielding an RMSD value of 0.95 ± 0.01 Å (below the 2.0 Å threshold). The binding energies of the eight tested compounds against COX-2 ranged from −11.1 to −7.3 kcal mol^{-1} (Table 6). The strongest interaction was observed for Nephtheasteroid A (−11.10 kcal mol^{-1}), surpassing celecoxib (−10.49 kcal mol^{-1}) and indomethacin (−10.50 kcal mol^{-1}) controls. Nebrosteroid J (−9.78 kcal mol^{-1}) and 24-norcholesterol (−9.55 kcal mol^{-1}) also showed favorable docking scores, whereas sesquiterpenes displayed moderate affinities (−8.38 to −7.34 kcal mol^{-1}). These results showed that

Table 6 Binding energies of candidate compounds against COX-2

Compounds	Binding energies (kcal mol^{-1})
1-Deoxymethylsphinganine	−7.34 ± 0.16
Guaianediol	−8.09 ± 0.01
Cyclocolorenone	−8.38 ± 0.00
Eudesma-4,7(11)-diene-8-one	−8.07 ± 0.00
Confertol	−7.74 ± 0.00
Nebrosteroid J	−9.78 ± 0.07
24-Norcholesterol	−9.55 ± 0.03
Nephtheasteroid A	−11.10 ± 0.09
Celecoxib (control)	−10.49 ± 0.03
Indomethacin (control)	−10.5 ± 0.00

Table 5 Common DEGs among the three datasets of GSE2322, GSE198326 and GSE40885

Common genes	log_2 FC (GSE2322)	log_2 FC (GSE198326)	log_2 FC (GSE40885)	Adj. *p*-value (GSE2322)	Adj. *p*-value (GSE198326)	Adj. *p*-value (GSE40885)	Expression
CCL20	7.95	6.74	3.57	1.28×10^{-7}	1.92×10^{-3}	5.49×10^{-4}	Upregulated
IL1B	3.67	5.34	2.67	1.28×10^{-7}	3.44×10^{-4}	2.08×10^{-5}	
IL1A	7.65	7.47	2.03	6.75×10^{-7}	3.11×10^{-5}	5.49×10^{-4}	
IL1RN	3.70	2.53	3.39	6.75×10^{-7}	6.49×10^{-4}	2.12×10^{-6}	
CXCL1	2.39	5.34	3.80	2.55×10^{-4}	4.74×10^{-5}	1.01×10^{-4}	
TNF	6.55	4.65	2.73	3.50×10^{-4}	4.11×10^{-5}	1.34×10^{-5}	
PTX3	3.53	5.26	4.31	3.37×10^{-3}	5.83×10^{-6}	2.72×10^{-5}	
FFAR2	2.29	2.71	2.15	5.47×10^{-3}	5.85×10^{-3}	5.55×10^{-5}	
GCH1	2.29	4.23	2.31	1.14×10^{-2}	4.52×10^{-4}	4.30×10^{-4}	
PTGS2	2.14	7.78	4.29	2.05×10^{-2}	2.68×10^{-7}	2.60×10^{-5}	

steroidal compounds, particularly nephtheasteroid A, nebrosteroid J, and 24-norcholesterol, could have promising COX-2 binding affinities with a predicted inhibitory potential (Fig. 7).

Interaction analysis revealed that nebrosteroid J, 24-norcholesterol, and nephtheasteroid A formed hydrogen bonds with Met522, a critical residue in pocket S2 of COX-2, with bond lengths of 2.34, 2.03, and 1.87 Å, respectively (Table 7). Additionally, hydrophobic stabilization was provided by van der Waals interactions with the residues Val116, Leu359, Leu531, Val523, Ala527, Tyr355, and Phe518.

Notably, the steroidal compounds extended into pocket S3, suggesting broader engagement within the cyclooxygenase channel (Fig. 8).

3.7. Absorption, distribution, metabolism, excretion, and toxicity (ADMET) prediction

The ADMET profiles of the eight docked compounds were predicted using the pkCSM platform. The results are summarized in Table 8. All compounds showed high human intestinal absorption (>88.99%) with cyclocolorenone being the highest (98.34%), whereas deoxymethylsphinganine exhibited the lowest (88.99%) absorption. For the blood–brain barrier (BBB) permeability, most compounds displayed positive log BB values, suggesting a potential to cross the BBB. Nephtheasteroid A showed the highest predicted BBB permeability (log BB = 0.799), while deoxymethylsphinganine and

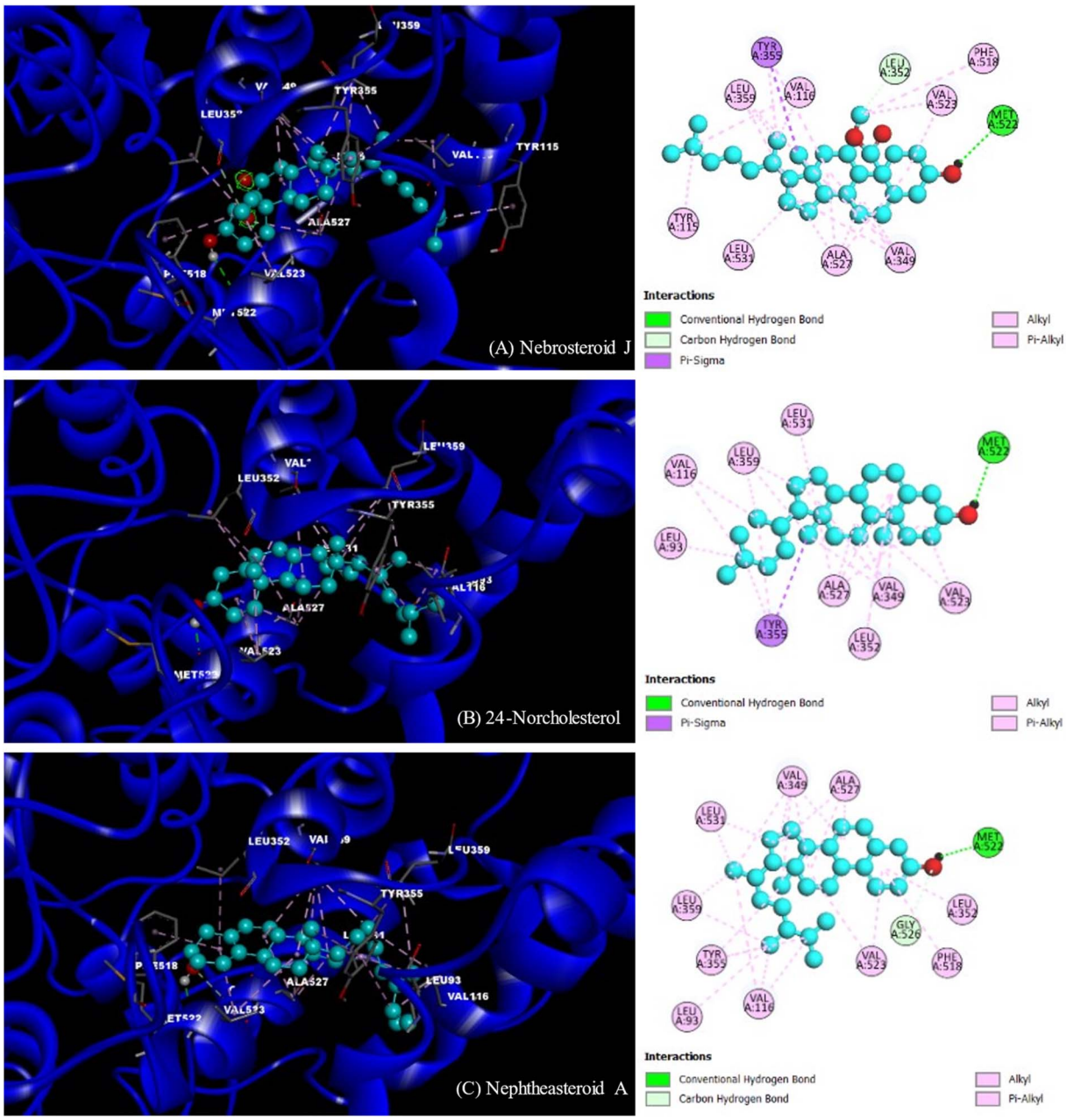

Fig. 7 Predicted binding modes of steroidal compounds within the COX-2 active site: (A) nebrosteroid J, (B) 24-norcholesterol, and (C) nephtheasteroid A, shown in 3D and 2D representations.

Table 7 Predicted COX-2 interactions of *L. savignyi* steroidal compounds

Compounds	Binding energies (kcal mol^{-1})	No. Of hydrogen bonds	Hydrogen bond residues	Bond distance (Å)	Hydrophobic pocket
Nebrosteroid J	−9.78 ± 0.07	1	Met522	2.34 ± 0.05	Val116, Leu359, Leu531, Val349, Val523, Ala527, Tyr355, Phe518 & Tyr115
24-Norcholesterol	−9.55 ± 0.03	1	Met522	2.03 ± 0.01	Val116, Leu359, Leu531, Val349, Val523, Ala527, Tyr355, Leu93, & Leu352
Nephtheasteroid A	−11.10 ± 0.09	1	Met522	1.87 ± 0.04	Val116, Leu359, Leu531, Val349, Val523, Ala527, Tyr355, Phe518, Leu93 & Leu352

nebrosteroid J displayed limited permeability (log BB < 0). CYP3A4 is a critical enzyme in hepatic drug clearance as it is responsible for the metabolism of approximately 60% of all clinically in-use drugs. 1-Deoxymethylsphinganine, nebrosteroid J, 24-norcholesterol, and nephtheasteroid A were predicted as CYP3A4 substrates, potentially affecting their metabolic stability and drug interactions. Most compounds did not inhibit other CYP isoforms, suggesting a low likelihood of interfering with CYP-mediated metabolism except for eudesma-4,7(11)-diene-8-one, which is predicted to inhibit CYP1A2, CYP2C19 and CYP2C9. All compounds were predicted to be safe (not mutagenic) according to the AMES test.

The molecular descriptors were computed using the SwissADME prediction tool. While most compounds adhered to Lipinski's rule, nebrosteroid J, 24-norcholesterol and nephtheasteroid A violated only one rule as they showed high lipophilicity with log *P* values of 5.34, 6.14, and 6.13, respectively, potentially compromising solubility and oral bioavailability (log *P* > 5) (Table 9).

The BOILED-Egg model (Fig. S4) was applied to evaluate the GIT absorption and BBB permeability of *L. savignyi* bioactive compounds based on their log *p* (O/W) (to reflect their lipophilicity) and topological polar surface area (TPSA to reflect their polarity). From the model, 24-norcholesterol and

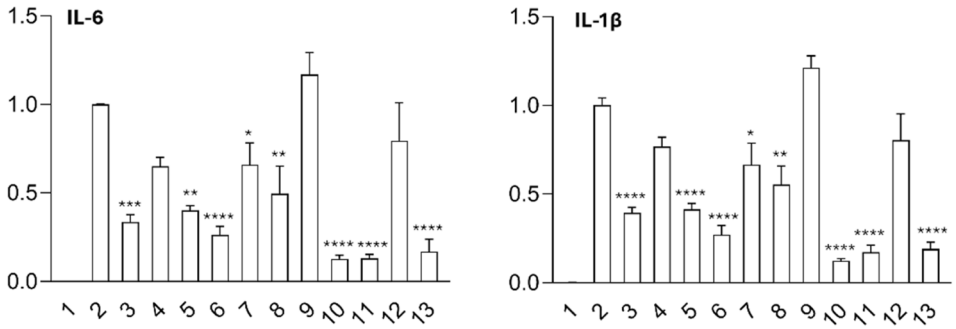

Fig. 8 qPCR analysis of IL-6 and IL-1β in human THP-1 cells: 1, DMSO; 2, DMSO + LPS as control; 3, NH20 + LPS; 4, ND50 + LPS; 5, NH50-1 + LPS; 6, NH50-4 + LPS; 7, NH70 + LPS, 8, NH80 + LPS; 9, NH100 + LPS; 10, ND90-1 + LPS; 11, ND90-3 + LPS; 12, methanol extract + LPS; and 13, hexane extract + LPS. A *p*-value of <0.05 was considered statistically significant. * *p*-value < 0.05, ** *p*-value ≤ 0.001, *** *p*-value < 0.0005, **** *p*-value < 0.0001.

Table 8 Prediction of the ADMET pharmacokinetics of *L. savignyi* bioactive compounds using pkCSM

	Absorption	Distribution	Metabolism							Excretion	Toxicity
			CYP								
			Substrate		Inhibitors						
Compounds	Intestinal absorption (% absorbed)	BBB permeability (log BB)	2D6	3A4	1A2	2C19	2C9	2D6	3A4	Total clearance (log mL min^{-1} kg^{-1})	AMES toxicity
Deoxymethylsphinganine	88.994	−0.397	No	Yes	Yes	No	No	Yes	No	1.429	No
Guaianediol	94.67	0.618	No	No	No	No	No	No	No	1.176	No
Cyclocolorenone	98.34	0.649	No	No	No	Yes	No	No	No	0.925	No
Eudesma-4,7(11)-diene-8-one	96.133	0.572	No	No	Yes	Yes	Yes	No	No	1.132	No
Confertol	94.971	0.486	No	No	No	No	No	No	No	0.861	No
Nebrosteroid J	96.895	−0.391	No	Yes	No	No	No	No	No	0.595	No
24-Norcholesterol	94.28	0.742	No	Yes	No	No	No	No	No	0.575	No
Nephtheasteroid A	95.753	0.799	No	Yes	No	No	No	No	No	0.676	No

Table 9 Prediction of the physicochemical properties of *L. savignyi* bioactive compounds based on the Lipinski's rule of five using the SwissADME prediction tool

	Physico-chemical properties					
Compounds	Molecular weight (Da)	Topological polar surface area (A)	LogP (O/W)	No. Of H-bond donors	No. Of H-bond acceptors	Lipinski violations
1-Deoxymethylsphinganine	271.48	46.25	3.77	2	2	0
Guaianediol	220.35	20.23	3.56	1	1	0
Cyclocolorenone	218.33	17.07	3.56	0	1	0
Eudesma-4,7(11)-diene-8-one	218.33	17.07	3.46	0	1	0
Confertol	236.35	29.46	2.74	1	2	0
Nebrosteroid J	428.65	46.53	5.34	1	3	1
24-Norcholesterol	372.63	20.23	6.14	1	1	1
Nephtheasteroid A	382.62	20.23	6.13	1	1	1

Table 10 Prediction of toxicity risks, drug-likeness, and drug scores using the OSIRIS software[a]

	Toxicity risks				Osiris calculations	
Compounds	MUT	TUMO	IRR	REP	DL	DS (%)
1-Deoxymethylsphinganine	Low	Low	Low	Low	−18.3	23
Guaianediol	Low	Low	Low	Low	−3.82	42
Cyclocolorenone	High	High	High	Low	−3.25	9
Eudesma-4,7(11)-diene-8-one	Low	Low	Low	Low	−2.4	42
Confertol	Low	Low	Low	Low	−0.39	63
Nebrosteroid J	Low	Low	High	Low	−1.96	12
24-Norcholesterol	Low	Low	Low	Low	−1.51	20
Nephtheasteroid A	Low	Low	Low	Low	−7.93	16

[a] MUT: mutagenic; TUMO: tumorigenic; IRR: irritant; REP: reproductive effect; DL: drug-likeness; DS: drug score.

nephtheasteroid A fall in the grey zone, which is outside the predictive zone of effective intestinal absorption and BBB penetration. Compounds located in the yellow zone, including 1-deoxymethylsphinganine, guaianediol, cyclocolorenone, eudesma-4,7(11)-diene-8-one, and confertol, are predicted to have higher potential for brain permeability, whereas those in the white region such as nebrosteroid J has higher probability of being absorbed by the gastrointestinal tract.

The OSIRIS model was employed to predict drug-likeness, drug score, and toxicity profiles for each compound. Since *in vitro* and *in vivo* toxicity studies are often time-consuming and costly, *in silico* models offer an effective alternative for early-stage evaluation of drug-likeness and toxicity, hence minimizing reliance on animal testing. Theoretical risks of toxicity of *L. savignyi* bioactive molecules were calculated using the Osiris software (Table 10) where the Osiris model flagged cyclocolorenone as highly mutagenic, tumorigenic, and irritant. Nebrosteroid J was predicted to be irritant, while the remaining compounds were non-toxic. Most compounds exhibited unfavorable drug-likeness except for confertol, 24-norcholesterol, and nebrosteroid J, as they were closer to zero.

3.8. qPCR of IL-6 and IL-1β

To validate the docking results, we examined the effects of the hexane extract of *L. savignyi* and its fractions on the expression of the pro-inflammatory cytokines IL-6 and IL-1β in LPS-primed THP-1 cells using qPCR. As shown in Fig. 8, the hexane extract exhibited stronger anti-inflammatory activity than the methanol extract, with subfractions ND90-1 and ND90-3 showing the most pronounced inhibitory effects on LPS-induced IL-6 and IL-1β upregulation.

Docking analyses predicted that major constituents enriched in ND90-1 and ND90-3 effectively interact with and inhibit COX-2. Given the known role of COX-2 in amplifying inflammatory signalling *via* the positive feedback regulation of cytokines, we further assessed whether COX-2 inhibition could be associated with reduced IL-6 and IL-1β expression.[64] The observed down-regulation of these cytokines is consistent with this mechanism and supports the involvement of COX-2-mediated pathways in the anti-inflammatory activity of the hexane subfractions.

4 Conclusions

The hexane fraction of the soft coral *Litophyton savignyi* displayed strong significant anti-inflammatory activity through reducing superoxide generation and elastase release compared to the methanol fraction which was inactive. The observed activity was attributed to the richness of the hexane fraction with steroids, which displayed comparable binding affinities on COX-2 receptor to indomethacin and celecoxib (control).

Author contributions

Shaimaa Fayez: investigation, methodology, software, supervision, data curation, writing-original draft. Karim Abed:

investigation, methodology, software, data curation, writing-original draft. Mostafa S. Moussa: investigation, methodology, software, data curation, writing-original draft. Lo-Yun Chen: methodology, data curation. Ting-Wei Liao: methodology, data curation. Tsong-Long Hwang: investigation, methodology, data curation. Po-Jen Chen: investigation, methodology, data curation. Mohamed El-Shazly: conceptualization, supervision, writing-review and editing. Kuei-Hung Lai: conceptualization, supervision, funding acquisition, writing-review and editing.

Conflicts of interest

The authors declare that they have no known competing financial interests or personal relationships that could have appeared to influence the work reported in this paper.

Data availability

The data supporting this article have been included as part of the supplementary information (SI). Supplementary information is available. See DOI: https://doi.org/10.1039/d5ra09089j.

Acknowledgements

This work was supported by the National Science and Technology Council of Taiwan (111-2320-B-038-040-MY3, 113-2628-B-038-009-MY3, 113-2321-B-255-001, and 114-2326-B-038-002-MY3) and the Ministry of Education (DP2-TMU-114-C-06).

Notes and references

1 A. U. Ahmed, *Front. Biol.*, 2011, **6**, 274–281.
2 R. Medzhitov, *Nature*, 2008, **454**, 428–435.
3 W. L. Lee and G. P. Downey, *Am. J. Respir. Crit. Care Med.*, 2001, **164**, 896–904.
4 J.-P. Motta, C. Rolland, A. Edir, A.-C. Florence, D. Sagnat, C. Bonnart, P. Rousset, L. Guiraud, M. Quaranta-Nicaise, E. Mas, D. Bonnet, E. F. Verdu, D. M. McKay, E. Buscail, L. Alric, N. Vergnolle and C. Deraison, *Mucosal Immunol.*, 2021, **14**, 667–678.
5 S. Nénan, E. Boichot, V. Lagente and C. P. Bertrand, *Mem. Inst. Oswaldo Cruz*, 2005, **100**, 167–172.
6 L. M. Coussens and Z. Werb, *Nature*, 2002, **420**, 860–867.
7 G. Döring, *Am. J. Respir. Crit. Care Med.*, 1994, **150**, S114–S117.
8 J. Mania-Pramanik, S. S. Potdar, A. Vadigoppula and S. Sawant, *J. Clin. Lab. Anal.*, 2004, **18**, 153–158.
9 W. C. Groutas, D. Dou and K. R. Alliston, *Expert Opin. Ther. Pat.*, 2011, **21**, 339–354.
10 K. M. Allam, A. I. M. Khedr, A. E. Allam, M. S. A. Abdelkader, E. S. Elkhayat and M. A. Fouad, *J. Adv. Biomedical Pharm. Sci.*, 2021, **4**, 124–133.
11 L. P. van Ofwegen, *ZooKeys*, 2016, 1–128, DOI: 10.3897/zookeys.567.7212.
12 X. Y. Yan, L. Zhang, Q. B. Yang, Z. Y. Ge, L. F. Liang and Y. W. Guo, *Mar. Drugs*, 2023, **21**, 523.
13 F. Amir, Y. Koay and W. S. Yam, *Trop. J. Pharmaceut. Res.*, 2012, **11**, 485.
14 J. Hu, B. Yang, X. Lin, X. Zhou, X. Yang, L. Long and Y. Liu, *Chem. Biodivers.*, 2011, **8**, 1011–1032.
15 O. H. Abdelhafez, J. R. Fahim, M. E. Rateb, C. J. Ngwa, G. Pradel, U. R. Abdelmohsen, S. Y. Desoukey and M. S. Kamel, *Nat. Prod. Res.*, 2022, **36**, 6464–6469.
16 K. Tani, T. Kamada, C.-S. Phan and C. S. Vairappan, *Nat. Prod. Res.*, 2019, **33**, 3343–3349.
17 N. H. Hassan, S. S. El-Hawary, M. Emam, M. A. Rabeh, U. R. Abdelmohsen and N. M. Selim, *ACS Omega*, 2022, **7**, 13808–13817.
18 T.-C. Tsai, Y.-T. Huang, S.-K. Chou, M.-C. Shih, C.-Y. Chiang and J.-H. Su, *Chem. Pharm. Bull.*, 2016, **64**, 1519–1522.
19 A. Ghallab, A. Mahdy, H. Madkour and A. Osman, *Egypt. J. Aquat. Biol. Fish.*, 2020, **24**, 125–145.
20 E. E. Dokalahy, H. R. El-Seedi and M. A. Farag, in. *Biodiversity and Chemotaxonomy*, ed. K. G. Ramawat, Springer International Publishing, Cham, 2019, pp. 55–85, DOI: 10.1007/978-3-030-30746-2_4.
21 I. Pountos, T. Georgouli, H. Bird and P. V. Giannoudis, *Int. J. Interferon Cytokine Mediat. Res.*, 2011, **3**, 19–27.
22 H. E. Vonkeman and M. A. F. J. van de Laar, *Semin. Arthritis Rheum.*, 2010, **39**, 294–312.
23 M. Wang, J. J. Carver, V. V. Phelan, L. M. Sanchez, N. Garg, Y. Peng, D. D. Nguyen, J. Watrous, C. A. Kapono, T. Luzzatto-Knaan, C. Porto, A. Bouslimani, A. V. Melnik, M. J. Meehan, W.-T. Liu, M. Crüsemann, P. D. Boudreau, E. Esquenazi, M. Sandoval-Calderón, R. D. Kersten, L. A. Pace, R. A. Quinn, K. R. Duncan, C.-C. Hsu, D. J. Floros, R. G. Gavilan, K. Kleigrewe, T. Northen, R. J. Dutton, D. Parrot, E. E. Carlson, B. Aigle, C. F. Michelsen, L. Jelsbak, C. Sohlenkamp, P. Pevzner, A. Edlund, J. McLean, J. Piel, B. T. Murphy, L. Gerwick, C.-C. Liaw, Y.-L. Yang, H.-U. Humpf, M. Maansson, R. A. Keyzers, A. C. Sims, A. R. Johnson, A. M. Sidebottom, B. E. Sedio, A. Klitgaard, C. B. Larson, C. A. Boya P, D. Torres-Mendoza, D. J. Gonzalez, D. B. Silva, L. M. Marques, D. P. Demarque, E. Pociute, E. C. O'Neill, E. Briand, E. J. N. Helfrich, E. A. Granatosky, E. Glukhov, F. Ryffel, H. Houson, H. Mohimani, J. J. Kharbush, Y. Zeng, J. A. Vorholt, K. L. Kurita, P. Charusanti, K. L. McPhail, K. F. Nielsen, L. Vuong, M. Elfeki, M. F. Traxler, N. Engene, N. Koyama, O. B. Vining, R. Baric, R. R. Silva, S. J. Mascuch, S. Tomasi, S. Jenkins, V. Macherla, T. Hoffman, V. Agarwal, P. G. Williams, J. Dai, R. Neupane, J. Gurr, A. M. C. Rodríguez, A. Lamsa, C. Zhang, K. Dorrestein, B. M. Duggan, J. Almaliti, P.-M. Allard, P. Phapale, L.-F. Nothias, T. Alexandrov, M. Litaudon, J.-L. Wolfender, J. E. Kyle, T. O. Metz, T. Peryea, D.-T. Nguyen, D. VanLeer, P. Shinn, A. Jadhav, R. Müller, K. M. Waters, W. Shi, X. Liu, L. Zhang, R. Knight, P. R. Jensen, B. Ø. Palsson, K. Pogliano, R. G. Linington, M. Gutiérrez, N. P. Lopes, W. H. Gerwick, B. S. Moore, P. C. Dorrestein and N. Bandeira, *Nat. Biotechnol.*, 2016, **34**, 828–837.

24 L.-F. Nothias, D. Petras, R. Schmid, K. Dührkop, J. Rainer, A. Sarvepalli, I. Protsyuk, M. Ernst, H. Tsugawa, M. Fleischauer, F. Aicheler, A. A. Aksenov, O. Alka, P.-M. Allard, A. Barsch, X. Cachet, A. M. Caraballo-Rodriguez, R. R. Da Silva, T. Dang, N. Garg, J. M. Gauglitz, A. Gurevich, G. Isaac, A. K. Jarmusch, Z. Kameník, K. B. Kang, N. Kessler, I. Koester, A. Korf, A. Le Gouellec, M. Ludwig, C. Martin H, L.-I. McCall, J. McSayles, S. W. Meyer, H. Mohimani, M. Morsy, O. Moyne, S. Neumann, H. Neuweger, N. H. Nguyen, M. Nothias-Esposito, J. Paolini, V. V. Phelan, T. Pluskal, R. A. Quinn, S. Rogers, B. Shrestha, A. Tripathi, J. J. J. van der Hooft, F. Vargas, K. C. Weldon, M. Witting, H. Yang, Z. Zhang, F. Zubeil, O. Kohlbacher, S. Böcker, T. Alexandrov, N. Bandeira, M. Wang and P. C. Dorrestein, *Nat. Methods*, 2020, **17**, 905–908.

25 A. BØYum, D. LØVhaug, L. Tresland and E. M. Nordlie, *Scand. J. Immunol.*, 1991, **34**, 697–712.

26 S.-C. Yang, P.-J. Chung, C.-M. Ho, C.-Y. Kuo, M.-F. Hung, Y.-T. Huang, W.-Y. Chang, Y.-W. Chang, K.-H. Chan and T.-L. Hwang, *J. Immunol.*, 2013, **190**, 6511–6519.

27 Y.-C. Chen, Y.-R. Lee, Y.-C. Chang, Y.-H. Wang, S.-Y. Fang, C.-H. Lin, P.-J. Chen and T.-L. Hwang, *J. Ethnopharmacol.*, 2025, **346**, 119653.

28 T. L. Hwang, Y. C. Su, H. L. Chang, Y. L. Leu, P. J. Chung, L. M. Kuo and Y. J. Chang, *J. Lipid Res.*, 2009, **50**, 1395–1408.

29 I. F. F. Benzie and J. J. Strain, *Anal. Biochem.*, 1996, **239**, 70–76.

30 M. A. van Agthoven, M. P. Barrow, L. Chiron, M.-A. Coutouly, D. Kilgour, C. A. Wootton, J. Wei, A. Soulby, M.-A. Delsuc, C. Rolando and P. B. O'Connor, *J. Am. Soc. Mass Spectrom.*, 2015, **26**, 2105–2114.

31 W. J. Griffiths, *Mass Spectrom. Rev.*, 2003, **22**, 81–152.

32 T. C. Tsai, Y. T. Huang, S. K. Chou, M. C. Shih, C. Y. Chiang and J. H. Su, *Chem. Pharmaceut. Bull.*, 2016, **64**, 1519–1522.

33 S. H. Xu, X. J. Liao and H. Lin, *Chin. J. Org. Chem.*, 2008, **28**, 861–964.

34 N. H. Hassan, S. S. El-Hawary, M. Emam, N. A. Safwat, M. A. Rabeh, U. R. Abdelmohsen and N. M. Selim, *Nat. Prod. Res.*, 2023, **37**, 3896–3901.

35 T. A. Mohamed, A. I. Elshamy, M. A. A. Ibrahim, M. A. M. Atia, R. F. Ahmed, S. K. Ali, K. A. Mahdy, S. O. Alshammari, A. M. Al-Abd, M. F. Moustafa, A. R. H. Farrag and M.-E. F. Hegazy, *Biomolecules*, 2021, **11**, 1247.

36 Y.-C. Huang, Z.-H. Wen, S.-K. Wang, C.-H. Hsu and C.-Y. Duh, *Steroids*, 2008, **73**, 1181–1186.

37 I. Sahidin, B. Sadarun, W. Wahyuni, L. O. Muhammad Julian Purnama, N. S. Rahmatika, M. H. Malaka, F. Malik and A. Fristiohady, *Pak J. Biol. Agric. Sci.*, 2023, **26**, 403–408.

38 J. H. Su, C. F. Dai, H. H. Huang, Y. C. Wu, P. J. Sung, C. H. Hsu and J. H. Sheu, *Chem. Pharmaceut. Bull.*, 2007, **55**, 594–597.

39 V. chandra sekhar, B. Sarvani and D. Rao, *Indian J. Chem., Sect. B:Org. Chem. Incl. Med. Chem.*, 2004, **35**, 1329–1331.

40 J. C. Coll, B. F. Bowden, D. M. Tapiolas, R. H. Willis, P. Djura, M. Streamer and L. Trott, *Tetrahedron*, 1985, **41**, 1085–1092.

41 M. R. Rao, K. V. Sridevi, U. Venkatesham, T. P. Rao, S. S. Lee and Y. Venkateswarlu, *J. Chem. Res.*, 2000, **2000**, 245–247.

42 S.-Y. Cheng, C.-F. Dai and C.-Y. Duh, *J. Nat. Prod.*, 2007, **70**, 1449–1453.

43 O. H. Abdelhafez, T. F. S. Ali, J. R. Fahim, S. Y. Desoukey, S. Ahmed, F. A. Behery, M. S. Kamel, T. A. M. Gulder and U. R. Abdelmohsen, *Int. J. Nanomed.*, 2020, **15**, 5345–5360.

44 T.-H. Hsiao, C.-S. Sung, Y.-H. Lan, Y.-C. Wang, M.-C. Lu, Z.-H. Wen, Y.-C. Wu and P.-J. Sung, *Mar. Drugs*, 2015, **13**, 3443–3453.

45 J.-Y. Pei, W.-F. Yu, J.-J. Zhang, T.-H. Kuo, H.-H. Chung, J.-J. Hu, C.-C. Hsu and K.-F. Yu, *Anal. Bioanal. Chem.*, 2022, **414**, 7635–7646.

46 L. Bao, H. Sun, Y. Zhao, L. Feng, K. Wu, S. Shang, J. Xu, R. Shan, S. Duan, M. Qiu, N. Zhang, X. Hu, C. Zhao and Y. Fu, *PLoS Pathog.*, 2023, **19**, e1011764.

47 D. Okutani, M. Lodyga, B. Han and M. Liu, *Am. J. Physiol. Lung Cell. Mol. Physiol.*, 2006, **291**, L129–L141.

48 S. E. Byeon, Y. S. Yi, J. Oh, B. C. Yoo, S. Hong and J. Y. Cho, *Mediat. Inflamm.*, 2012, **2012**, 512926.

49 R. Li, J. Xie, W. Xu, L. Zhang, H. Lin and W. Huang, *Reprod. Biol.*, 2022, **22**, 100696.

50 J. Hellmann, Y. Tang, M. J. Zhang, T. Hai, A. Bhatnagar, S. Srivastava and M. Spite, *Prostag. Other Lipid Mediat.*, 2015, **116–117**, 49–56.

51 Y. Xu, L. S. Peng, C. Q. Xiao, Y. Zhou, Q. S. Wang and H. Fu, *Brain Res. Bull.*, 2025, **222**, 111221.

52 X. Ding, C. Meng, H. Dong, S. Zhang, H. Zhou, W. Tan, L. Huang, A. He, J. Li, J. Huang, W. Li, F. Zou and M. Zou, *BMJ Open Diabetes Res. Care*, 2022, **10**, e002579.

53 A. Vallée and Y. Lecarpentier, *Front. Immunol.*, 2018, **9**, 745.

54 K. A. Smith, G. B. Waypa and P. T. Schumacker, *Redox Biol.*, 2017, **13**, 228–234.

55 L. Y. Yu-Lee, *Recent Prog. Horm. Res.*, 2002, **57**, 435–455.

56 J.-S. Jung, M.-J. Choi, Y. Y. Lee, B.-I. Moon, J.-S. Park and H.-S. Kim, *J. Agric. Food Chem.*, 2017, **65**, 373–382.

57 D. R. Korns, S. C. Frasch, R. Fernandez-Boyanapalli, P. M. Henson and D. L. Bratton, *Front. Immunol.*, 2011, 2–2011.

58 M. R. Elliott, K. M. Koster and P. S. Murphy, *J. Immunol.*, 2017, **198**, 1387–1394.

59 Y. Ge, M. Huang and Y.-m. Yao, *Front. Cell Dev. Biol.*, 2022, 10–2022.

60 L. Huang and L. Fu, *Acta Pharm. Sin. B*, 2015, **5**, 390–401.

61 X. Pan, X. Cao, N. Li, Y. Xu, Q. Wu, J. Bai, Z. Yin, L. Luo and L. Lan, *Inflammation Res.*, 2014, **63**, 597–608.

62 A. Sarapultsev, E. Gusev, M. Komelkova, I. Utepova, S. Luo and D. Hu, *Mol. Biomed.*, 2023, **4**, 40.

63 S. Schenone, F. Manetti and M. Botta, *Curr. Pharm. Des.*, 2007, **13**, 2118–2128.

64 J. Zhu, S. Li, Y. Zhang, G. Ding, C. Zhu, S. Huang, A. Zhang, Z. Jia and M. Li, *Am. J. Transl. Res.*, 2018, **10**, 966–974.